Int J Fract (2019) 220:45–83
https://doi.org/10.1007/s10704-019-00396-4

ORIGINAL PAPER

Analysis of self-similar rate-dependent interfacial crack propagation in mode II

Milan Jirásek · **Olivier Allix**

Received: 21 March 2019 / Accepted: 19 October 2019 / Published online: 5 November 2019

Abstract The present study analyzes the fundamental properties of a rate-dependent cohesive model applied to the description of dynamic mode-II crack propagation. To make a semi-analytical treatment possible, the idealised problem of a crack along the interface between a semi-infinite elastic layer and a rigid substrate is considered. Solutions corresponding to the propagation of the crack tip at a constant speed are constructed. Using asymptotic properties of the solution far from the crack tip allows obtaining the complete solution of the boundary value problem by direct integration without iterations, using a specific form of the shooting method. By conversion of the problem to dimensionless variables, the behavior of the system for all possible crack velocities and arbitrary combinations of material and geometric parameters can be characterized. The dependence of fracture energy and other important characteristics on model parameters and the crack speed can then be analyzed. Even if the approach is applied to a specific form of damage rate dependence and motivated by the analysis of delamination propagation, the same technique could be used for other classes of interfacial cohesive rate-dependent models.

M. Jirásek (✉)
Fac Civil Engn, Dept Mech, Czech Tech Univ, Thákurova 7, 16629 Prague 6, Czech Republic
e-mail: milan.jirasek@fsv.cvut.cz

O. Allix
LMT, ENS Paris-Saclay/CNRS/Université Paris-Saclay, 61 avenue du Président Wilson, 94235 Cachan Cedex, France
e-mail: olivier.allix@ens-paris-saclay.fr

Keywords Rate-dependent damage model · Mode-II interfacial crack · Dynamic self-similar propagation · Semi-analytic solution · Direct shooting method

1 Introduction

The description of rate effect on delamination in polymeric interfaces is a controversial issue. For adhesive bond joints, a decrease of the critical energy release rate in mode I, G_{1c}, is reported in Karac et al. (2011), while in Burak and Coker (2016) an increase of G_{1c} is reported in the case of a three-point impact bending test that exemplifies low-speed mode-I dynamic fracture. Moreover, in Smiley and Pipes (1987a) a constant value of G_{1c} followed by a decrease of this value at high opening rates is reported. For mode-II solicitations, the issue is also controversial. In Cantwell (1997), an increase of G_{2c} depending on the fiber type is reported for the same PEEK matrix, while a negative rate effect is reported in Smiley and Pipes (1987b) for the same type of matrix, and no variation of G_{2c} is reported in Tsai et al. (2001). This shows that the physics of delamination in dynamics is not fully understood yet and the experimental methodology for properly studying those effects still remains a challenge.

The question of rate dependence of crack propagation also arises for metallic materials, leading to the need for a rate-dependent cohesive model. It has been reported by numerous authors that the use of rate-independent cohesive models results into crack speeds

much higher than those measured or expected (see, e.g., Valoroso et al. 2014). In the case of delamination mode-II propagation, the same conclusion was made in Guimard et al. (2009). A well-known possible explanation of this phenomenon can be found in Ravi-Chandar and Knauss (1984). When the crack speed increases, the development of secondary microcracks (i) diminishes the energy available as a driving force of the main crack, and (ii) for the same main crack increases the total area of new surfaces and thus possibly the macroscopic critical energy release rate. This phenomenon was studied in Zhou et al. (2005) and motivated the authors to propose a rate-dependent cohesive crack model.

In Allix and Deü (1997), a bounded-rate damage model was proposed as a possible regularisation tool for damage in dynamics. This approach was further developed in Allix (2013). In Guimard et al. (2009), the same approach was used to reproduce the crack speed obtained in a pure mode-II delamination test. Some fitting was suggested to possibly associate the proposed bounded-rate model with an expression of the resulting critical energy release rate as a function of the crack speed. This fitting was made within a limited range of crack velocities and thus is debatable.

All these considerations have motivated the present paper, aiming at a deeper examination of the relation between a rate-dependent cohesive model and its fracture mechanics counterpart in dynamics. To make a semi-analytic treatment possible, the idealised problem of delamination of an infinitely long layer from a rigid substrate is considered, and solutions corresponding to propagation of the crack tip (delamination front) at a constant velocity are constructed. The delaminating layer is modelled as an elastic bar connected to the substrate by an inelastic interface, which is described by a cohesive zone model.

Mathematical description of the above problem leads to a set of ordinary differential equations, which is simplified by conversion to dimensionless variables. The solution is then constructed using a specific form of the shooting method, adapted such that the solution satisfying all boundary conditions is obtained without iterations. This efficient numerical technique permits simple and fast calculations, and the dependence of the physical characteristics of the system on the choice of model parameters can be evaluated. Such calculations elucidate the role of individual parameters and facilitate identification of optimal parameter values from experimental data. They also reveal some of the fundamental features of the model, including its scaling and asymptotic properties. Let us note that a discussion of the numerical difficulties encountered when trying to solve such problem was presented in Kubair et al. (2003) for the more complex case of mode-III crack propagation in a two-dimensional domain. A Riemann–Hilbert approach was applied to deal with those difficulties. We are able to use a much simpler approach here, mainly due to the simplified one-dimensional modelling of the problem.

The paper is organised as follows:

In Sect. 2, basic equations describing a simplified model of mode-II delamination are presented. The main ingredients of a rate-independent interfacial damage model, which will serve as a starting point for later extensions to rate-dependent formulations, are detailed. Moreover, an energetic analysis is performed, resulting into the definition of the rate at which energy is consumed by the delamination process.

In Sect. 3, the hypothesis of a "dynamic steady process" is introduced. This hypothesis allows the reduction of the problem to a set of two coupled ordinary differential equations. In this context, a continuation of the energetic analysis leads to the definition of the rate-dependent fracture energy, considered here as functions of the crack speed. Other global characteristics include the force needed to drive the crack and the speed at which the end section moves.

In Sect. 4, analytical solutions for two versions of the rate-independent damage model are derived. This allows to set a basis of comparison for rate effects studied in the following sections.

In Sect. 5, bounded-rate damage models studied in the paper are presented. A new interpretation clarifying the formulation of the model is proposed and discussed.

In Sect. 6, a special form of the shooting method based on a finite difference scheme is introduced. Its purpose is to deal with rate-dependent models when no closed-form solutions are available. An asymptotic development provides the boundary conditions at an arbitrary location far from the crack tip. Then, integrating backward in dimensionless space, the complete solution is determined without iterations.

In Sect. 7, the method is applied to a particular case studied in Guimard et al. (2009) where finite elements were used to approximate experimental results. In the present work, numerical solutions are computed over the whole range of possible crack speeds. This allows in particular to show that the fitting of the critical energy

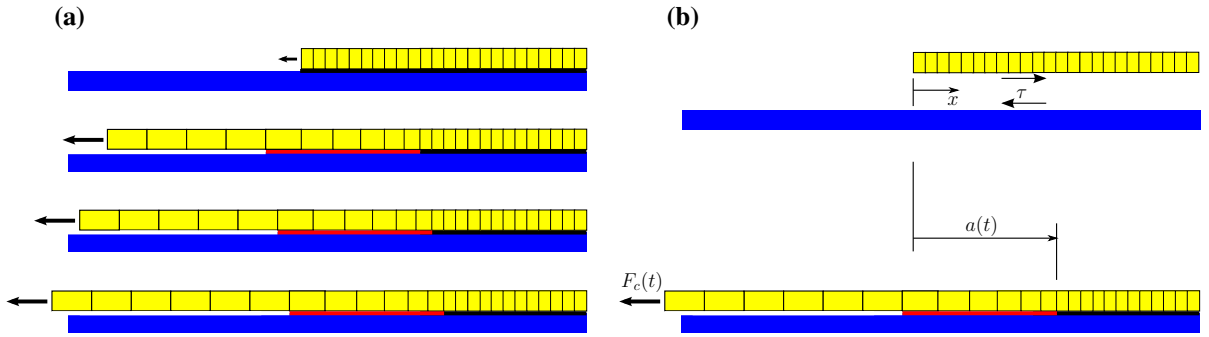

Fig. 1 **a** Schematic representation of the delamination process: elastic layer (yellow) attached to a rigid substrate (blue) by an interface (black) that gets damaged (red) up to full decohesion (white gap), **b** choice of coordinate system and sign convention for the interfacial shear stress τ and applied force F_c

release rate proposed in Guimard et al. (2009) is valid for low crack speeds only, and to demonstrate that the rate-dependent formulation does not lead to any reduction of the theoretical limit of the crack speed. The example also permits to characterize the influence of inertia forces separately from the effects caused by the rate-dependent extension of the cohesive damage law.

In Sect. 8, the governing equations are converted into a dimensionless form, which makes it possible to characterize all possible cases by varying only two dimensionless parameters. Possible identification of parameters of the rate-dependent model based on self-similar crack tests at different crack speeds is discussed.

In Sect. 9, we examine the effect of rate dependence over a wide range of crack speeds, by comparing the results to those obtained with the rate-independent model. This is done for two specific forms of the damage law, in order to study the effect of the shape of the rate-independent traction-displacement curve, with all other main characteristics of the model being fixed. In order to obtain closed-form estimates, two extreme cases are further analysed: the case of low crack speeds, and the case of crack speeds close to the elastic wave speed.

In the conclusion section, based on the obtained results and on the questions raised in the paper, further research directions are proposed.

2 Model for pure mode-II delamination

Delamination in pure mode II is studied here using an idealised model of an elastic layer bonded to a rigid substrate; see Fig. 1a. The layer is modelled as a semi-infinite bar with rectangular cross section of width b and depth h, and the material of the layer is characterised by Young's modulus E and mass density ρ. The depth is considered as very small, so that bending effects can be neglected and the layer can be treated as a bar under axial tension. Interaction between the bar and the substrate is described by shear stress τ, which is linked by a nonlinear and possibly rate-dependent cohesive law to the relative displacement between the bar and the substrate.

The sign convention is sketched in Fig. 1b. The origin of the coordinate axis x is placed at the initial location of the bar end section, and the axis is positively oriented to the right, so that the semi-infinite bar corresponds to the interval $[0, \infty)$. The shear stress τ arising at the interface is positive if it acts on the bar to the right and on the substrate to the left. The displacement of the bar, u, is positive to the right, but the displacement jump $[\![u]\!]$ is considered as the difference between the (zero) displacement of the substrate and the displacement of the bar, and thus is equal to $-u$. With this convention, a positive displacement jump leads to a positive shear stress. The external force F_c applied at the end section is considered as positive to the left.

2.1 Basic equations

For the present simple model, the equation of motion (momentum balance equation) reads

$$N_{,x}(x,t) + b\tau(x,t) - bh\rho u_{,tt}(x,t) = 0 \qquad (1)$$

where N is the normal force in the bar (normal stress times the sectional area), τ is the cohesive shear stress in

the interface, bh is the sectional area, and u is the axial displacement. Subscript x after a comma denotes the derivative with respect to the spatial coordinate x, and subscript tt after a comma denotes the second derivative with respect to time t.

The normal force in the bar is linked to the axial strain $\varepsilon = u_{,x}$ by the elastic law

$$N = Ebh\varepsilon = Ebhu_{,x} \tag{2}$$

and the shear stress at the interface is governed by the cohesive law

$$\tau = k\,(1 - D)\,[\![u]\!] = -k\,(1 - D)\,u \tag{3}$$

in which k is the tangential elastic stiffness of the interface, D is the damage variable, and $[\![u]\!] = 0 - u = -u$ is the tangential displacement jump. Substituting (2) and (3) into (1), we obtain

$$\begin{aligned} &Ebhu_{,xx}(x,t) - bh\rho u_{,tt}(x,t) \\ &\quad = bk\,(1 - D(x,t))\,u(x,t) \end{aligned} \tag{4}$$

When the end section of the bar is pulled as schematically shown in Fig. 1a, the displacement jump increases and damage is induced at the interface. At points where the displacement jump $[\![u]\!]$ exceeds a certain limit u_f, no shear stress is transmitted and the interface can be considered as fully debonded. The point that separates the fully debonded zone from the cohesive zone will be referred to as the crack tip, even though we do not deal here with an opening crack but with mode-II delamination.

To obtain a complete description of the inelastic processes taking place at the damaging interface, cohesive law (3) must be supplemented by an evolution law for the damage variable. For **monotonic loading** and a **rate-independent damage model**, the damage variable is considered simply as a function of the displacement jump:

$$D = g([\![u]\!]) = g(-u) \tag{5}$$

2.2 Chosen expressions for the rate-independent damage models

The damage function g affects the shape of the resulting cohesive curve (stress-displacement diagram). In Guimard et al. (2009), a power law with exponent n was used. To make sure that damage cannot become larger than 1, such a law would need to be written in the form

$$g([\![u]\!]) = \begin{cases} \left(\dfrac{[\![u]\!]}{u_f}\right)^n & \text{if } [\![u]\!] \le u_f \\ 1 & \text{if } u_f < [\![u]\!] \end{cases} \tag{6}$$

Here, u_f is the displacement jump at which the cohesive stress vanishes. For $n = 1$, the dependence of damage on displacement jump is linear and the resulting cohesive curve has a parabolic shape, as shown in Fig. 2a.

According to the power law (6), nonzero damage is induced by an arbitrarily small displacement jump and the stress-displacement diagram is nonlinear from the very beginning. Sometimes it may be preferable to use a linear elastic law before a certain damage threshold is reached. A simple example is provided by a model with linear elasticity followed by linear softening, as shown in Fig. 2b. The corresponding damage function g is given by

$$g([\![u]\!]) = \begin{cases} 0 & \text{if } [\![u]\!] \le u_p \\ 1 - \dfrac{u_p}{[\![u]\!]}\dfrac{u_f - [\![u]\!]}{u_f - u_p} & \text{if } u_p < [\![u]\!] \le u_f \\ 1 & \text{if } u_f < [\![u]\!] \end{cases} \tag{7}$$

where u_p is the displacement jump at the onset of damage, which at the same time corresponds to the peak of the stress-displacement diagram.

For monotonic loading, the stress can be expressed as a unique function of the displacement jump, given in general by $\tau([\![u]\!]) = k(1 - g([[u]]))[\![u]\!])$, as follows from (3) combined with (5). For the power law (6), this function is continuously differentiable for $0 < [\![u]\!] < u_f$ and it is easy to show that the maximum stress

$$\tau_{\max} = \frac{knu_f}{(n+1)^{n+1}} \tag{8}$$

is attained at $[\![u]\!] = u_f/(n+1)^{1/n}$. For damage law (7) that leads to linear softening, the maximum stress $\tau_{\max} = ku_p$ is attained right at the onset of damage, i.e., at $[\![u]\!] = u_p$.

The dependence of shear stress τ on the displacement jump $[\![u]\!]$ is graphically represented by the stress-displacement diagram (also called the cohesive curve);

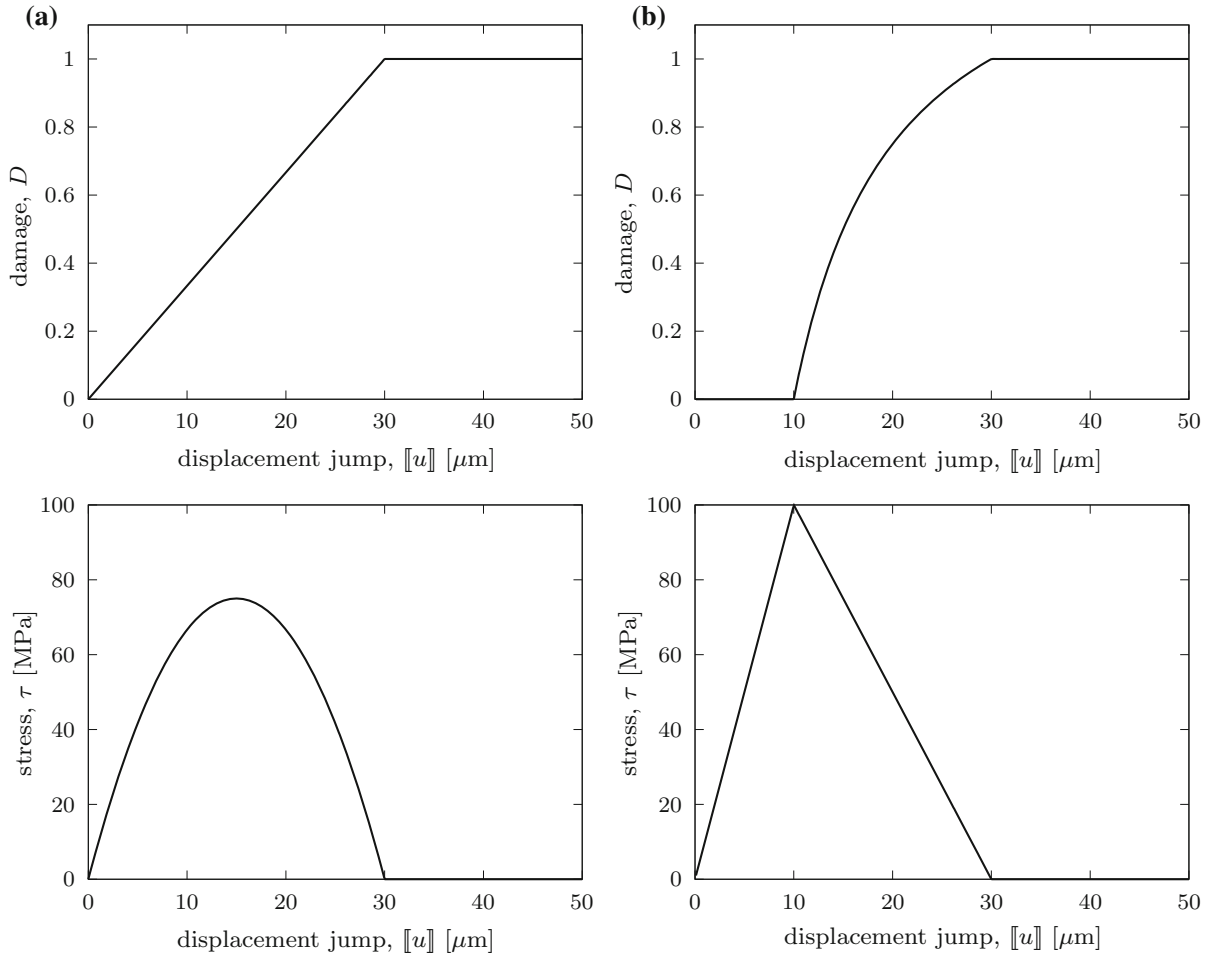

Fig. 2 Dependence of damage (top) and shear stress (bottom) on displacement jump for (a) model based on (6) with $n = 1$, (b) model based on (7) with $u_p = u_f/3$; in both cases, $u_f = 30$ µm and $k = 10 \cdot 10^{12}$ N/m^3

see the bottom part of Fig. 2. For power law (6) with $n = 1$, this diagram has a parabolic shape, and for damage law (7) it has a triangular shape. Therefore, we will refer to the corresponding models using the expressions "parabolic" and "triangular". The area under the cohesive curve corresponds to the work per unit interface area supplied to the interface during a complete failure process. On the macroscopic scale, this work of separation (or work of fracture) is not recoverable. For rate-independent models, the energy needed for full delamination of a unit area of the interface will be called the static fracture energy and denoted as G_{c0}. By integrating function $\tau([\![u]\!])$ from 0 to u_f, we obtain

$$G_{c0} = \frac{knu_f^2}{2(n+2)} \tag{9}$$

for damage law (6) and

$$G_{c0} = \tfrac{1}{2} k u_p u_f \tag{10}$$

for damage law (7). In fact, in the latter case it is sufficient to directly express the area of a triangle of base u_f and height ku_p. Parameters for the examples of cohesive curves in Fig. 2 have been selected such that both models are characterized by the same values of $k = 10 \cdot 10^{12}$ N/m^3, $u_f = 30$ µm and $G_{c0} = 1500$ J/m^2, which are the reference parameters specified in Table 1.

It would be easy to generalize the rate-independent formulation to the case of **non-monotonic loading**. The dependence of the damage variable D on the current value of displacement jump $[\![u]\!]$ would be replaced

Table 1 Reference values of primary material parameters and the corresponding derived parameters

Parameter	Value	Unit
(a) primary		
E	151×10^9	Pa
h	1.56×10^{-3}	m
ρ	1600	kg/m^3
k	10×10^{12}	N/m^3
G_{c0}	1500	J/m^2
τ_c	5×10^{-6}	s
A_c	3	–
(b) derived		
$c = \sqrt{E/\rho}$	9715	m/s
$u_f = \sqrt{6G_{c0}/k}$	30×10^{-6}	m
$l_0 = \sqrt{Eh/k}$	4.85×10^{-3}	m
$\lambda_0 = l_0/(c\tau_c)$	0.1	–

by the dependence of D on a history variable κ which represents the maximum value of the magnitude of displacement jump reached so far. For the present purpose, such modification is not needed. Extension to a **rate-dependent formulation** will be discussed in Sect. 5. Here it is sufficient to note that the delayed damage approach used in this paper will be based on a damage evolution equation of the general form

$$D_{,t} = f(\llbracket u \rrbracket, D) \tag{11}$$

where f is a non-negative continuous function that vanishes if $g(\llbracket u \rrbracket) \le D$.

2.3 Energetic aspects

It is instructive to look in detail at the energy balance. The external work supplied by the applied end force F_c is partially converted into potential and kinetic energy, and the remaining energy is available as a driving "force" of the damage process on the interface. This consideration motivates the definition of the dynamic energy release rate,

$$P_{rel} = F_c v_c - \dot{E}_{pot} - \dot{E}_{kin} \tag{12}$$

as the difference between the external power input provided by the end force $F_c(t) = N(0,t) = Ebhu_{,x}(0,t)$ that moves at speed $v_c(t) = -u_{,t}(0,t)$ and the time derivative of the sum of potential and kinetic energy. Superposed dot indicates differentiation with respect to time (for functions that depend on time only). The potential energy

$$E_{pot} = bh \int_0^\infty \tfrac{1}{2} E u_{,x}^2 \,\mathrm{d}x + b \int_0^\infty \tfrac{1}{2}(1-D) k u^2 \,\mathrm{d}x \tag{13}$$

is obtained by summing the contribution of the strain energy of the elastic bar and the energy stored in the damageable interface. The kinetic energy

$$E_{kin} = bh \int_0^\infty \tfrac{1}{2} \rho u_{,t}^2 \,\mathrm{d}x \tag{14}$$

resides exclusively in the elastic bar because the interface is massless and the rigid substrate is at rest.

Working out the time derivatives,

$$\dot{E}_{pot} = bh \int_0^\infty E u_{,x} u_{,xt} \,\mathrm{d}x + b \int_0^\infty (1-D) k u u_{,t} \,\mathrm{d}x - b \int_0^\infty \tfrac{1}{2} D_{,t} k u^2 \,\mathrm{d}x \tag{15}$$

$$\dot{E}_{kin} = bh \int_0^\infty \rho u_{,t} u_{,tt} \,\mathrm{d}x \tag{16}$$

integrating by parts,

$$\int_0^\infty E u_{,x} u_{,xt} \,\mathrm{d}x = \left[E u_{,x} u_{,t} \right]_{x=0}^\infty - \int_0^\infty E u_{,xx} u_{,t} \,\mathrm{d}x \tag{17}$$

and recalling that $Ebhu_{,x}(0,t) = F_c(t)$ and $u_{,t}(0,t) = -v_c(t)$ and that the strain $u_{,x}$ and velocity $u_{,t}$ tend to zero as $x \to \infty$, we can transform expression (12) for the dynamic energy release rate into

$$P_{rel} = b \int_0^\infty \left[Ehu_{,xx} - \rho h u_{,tt} - (1-D) k u \right] u_{,t} \,\mathrm{d}x + b \int_0^\infty \tfrac{1}{2} k u^2 D_{,t} \,\mathrm{d}x \tag{18}$$

Eq. (4), which follows from the momentum balance equation (1) combined with constitutive equations (2)–(3), implies that the expression in the brackets in the first integral on the right-hand side of (18) vanishes, and so the expression for the dynamic energy release rate reduces to

$$P_{rel} = b \int_0^\infty \tfrac{1}{2} k u^2 D_{,t} \,\mathrm{d}x \tag{19}$$

Here, $ku^2/2$ can be interpreted as the interfacial damage energy release rate per unit area (it corresponds to the negative derivative of the interfacial stored energy density with respect to the damage variable).

The dynamic energy release rate, P_{rel}, has been introduced in (12) as the difference between the external power, $F_c v_c$, and the rate of change of the kinetic and potential energy, $\dot{E}_{kin} + \dot{E}_{pot}$. The energy conservation law implies that the released energy must be equal to the energy spent by the delamination process, i.e., to the work of fracture. Therefore, we will use the relation

$$P_{fra} = P_{rel} \tag{20}$$

and from now on we will replace the dynamic energy release rate P_{rel} in the previously derived equations by the power of fracture, P_{fra}. This may seem to be just a formalistic exercise, but it is good to bear in mind that P_{rel} is the rate at which energy is released during the evolution of the system while P_{fra} is the rate at which energy is consumed by the delamination process.

3 Self-similar dynamic delamination process

3.1 Reduction to ordinary differential equation

Let us now analyze a "dynamic steady process", i.e., a self-similar delamination process in which the crack tip moves at a constant velocity $\dot{a}$ and all spatial fields travel with the crack at the same velocity. Such behavior can be expected to be approached asymptotically in a transitional process with a constant applied displacement rate at the end section. Due to self-similarity, the dependence of all variables on x and t can be replaced by a dependence on the transformed variable $\hat{x}(x,t) = x - a_0 - \dot{a}t$ where a_0 indicates the crack tip position at time $t = 0$. We can then write

$$u(x,t) = \hat{u}(\hat{x}(x,t)) \tag{21}$$

$$D(x,t) = \hat{D}(\hat{x}(x,t)) \tag{22}$$

$$u_{,xx}(x,t) = \hat{u}''(\hat{x}(x,t)) \tag{23}$$

$$u_{,tt}(x,t) = \dot{a}^2\hat{u}''(\hat{x}(x,t)) \tag{24}$$

where $\hat{u}''$ denotes the second derivative of $\hat{u}$ with respect to $\hat{x}$. Partial differential equation (4) can now be transformed into the ordinary differential equation

$$bh\left(E - \rho\dot{a}^2\right)\hat{u}''(\hat{x}) = bk\left(1 - \hat{D}(\hat{x})\right)\hat{u}(\hat{x}) \tag{25}$$

Note that a hat over a symbol is used here for functions that describe the dependence of a quantity on the transformed variable $\hat{x}$. Ordinary derivatives of functions of one variable will be denoted by primes, independently of the type of independent variable (argument). For instance, if $\hat{u}$ is a function of $\hat{x}$, we use $\hat{u}'$ for $\mathrm{d}\hat{u}/\mathrm{d}\hat{x}$.

In the **cracked zone** (i.e., fully delaminated zone) with $\hat{x} < 0$, we have $\hat{D} = 1$ and (25) reduces to

$$\hat{u}''(\hat{x}) = 0 \tag{26}$$

which implies that $\hat{u}$ must be a linear function of $\hat{x}$. Due to continuity of displacements and of the normal force, function $\hat{u}$ and its derivative $\hat{u}'$ must by continuous at $\hat{x} = 0$, and so the values of $\hat{u}(0)$ and $\hat{u}'(0)$ uniquely determine the linear function $\hat{u}(\hat{x})$ for $\hat{x} \le 0$. Denoting $\hat{u}(0) = u_c$ and $\hat{u}'(0) = \varepsilon_c$, we can write the solution in the cracked zone as

$$\hat{u}(\hat{x}) = u_c + \varepsilon_c\hat{x} \qquad \text{for } \hat{x} \le 0 \tag{27}$$

The values of u_c and ε_c will be found by solving the problem for $\hat{x} \ge 0$ and imposing continuous differentiability at $\hat{x} = 0$. Once we get these values, the displacement field in the cracked zone, considered as function of the spatial coordinate and time, can be expressed as

$$\begin{aligned} u(x,t) &= \hat{u}\,(x - a_0 - \dot{a}t) \\ &= u_c - \varepsilon_c a_0 + \varepsilon_c x - \varepsilon_c \dot{a}t \qquad \text{for } x \le a_0 + \dot{a}t \end{aligned} \tag{28}$$

The corresponding strain

$$\varepsilon(x,t) = u_{,x}(x,t) = \varepsilon_c \tag{29}$$

is constant, and so the normal force

$$N(x,t) = Ebh\varepsilon(x,t) = Ebh\varepsilon_c \tag{30}$$

is also constant (independent of the spatial coordinate and of time). Consequently, the force

$$F_c(t) = N(0,t) = Ebh\varepsilon_c \tag{31}$$

needed to propagate the crack at a constant velocity is constant in time, as may have been expected.

The velocity in the cracked zone,

$$v(x,t) = u_{,t}(x,t) = -\varepsilon_c\dot{a} \tag{32}$$

is also constant. The negative sign means that cross sections in the cracked zone move to the left. The magnitude of their velocity, $v_c = |v(0,t)| = \varepsilon_c \dot{a}$, is the product of the strain in the cracked zone and the crack speed.

Let us emphasize that equations (26)–(30) and (32) are valid exclusively in the fully delaminated zone. In the **damage process zone**, the damage variable grows from 0 to 1 and the solution is more complicated. The displacement and damage fields must be obtained by solving Eq. (25) combined with the damage evolution law and with appropriate boundary conditions. The crack tip is characterized by $D = 1$, and so we need to set $\hat{D}(0) = 1$. As $\hat{x} \to \infty$, the displacement should tend to zero, and the damage as well.

3.2 Energetic aspects revisited

Equation (19) has general validity and indicates that, locally, the energy release rate per unit area of the interface is given by the product of $ku^2/2$ and the damage rate. In general, the total energy release rate P_{rel} would depend on the current distribution of displacement and damage rate in space and would vary in time. In the presently considered special case, when the damage process zone propagates in a self-similar manner, each interface point is subjected to the same displacement and damage evolution, just shifted in time depending on the spatial position. Consequently, the dynamic energy release rate is constant in time and can be uniquely linked to one parameter that characterizes the rate of the process, e.g., to the crack speed $\dot{a}$. In view of Eq. (20), supported by the discussion at the end of Sect. 2.3, we will replace P_{rel} by P_{fra} and interpret the result in terms of the work of fracture.

Substituting $D_{,t} = -\dot{a}\hat{D}'$ into (19), replacing P_{rel} by P_{fra} and taking into account that $\hat{D}'(\hat{x}) = 0$ for $\hat{x} < 0$, we obtain

$$P_{fra} = -b \int_0^\infty \tfrac{1}{2} k \hat{u}^2 \hat{D}' \, \mathrm{d}\hat{x} \; \dot{a} = G_c b \dot{a} \tag{33}$$

where

$$G_c = -\int_0^\infty \tfrac{1}{2} k \hat{u}^2 \hat{D}' \, \mathrm{d}\hat{x} \tag{34}$$

can be considered as the rate-dependent fracture energy. In contrast to the static fracture energy G_{c0} introduced in Sect. 2.2, G_c is not a material property—it depends on the crack speed, $\dot{a}$.

Based on (34), the rate-dependent fracture energy can be evaluated from the damage distribution $\hat{D}(\hat{x})$, constructed for the given crack speed by solving equation (25) combined with the damage evolution equation that follows from (5) or (11), rewritten in terms of $\hat{u}$ and $\hat{D}$. However, it is also possible to compute G_c from the local value of strain at the crack tip. This can be shown by going back to (12)–(14) and making use of the special form of the self-similar solution. The power input provided by the end force $F_c = Ebh\varepsilon_c$ that moves at speed $v_c = \varepsilon_c \dot{a}$ is given by

$$F_c \times v_c = Ebh\varepsilon_c \times \varepsilon_c \dot{a} = Ebh\varepsilon_c^2 \dot{a} \tag{35}$$

The fully delaminated part of the bar moves at constant strain and constant velocity, and so its strain energy as well as kinetic energy remains constant. However, during a time interval $\mathrm{d}t$, the previously existing fully delaminated part gets longer by a new segment of length $\dot{a}\,\mathrm{d}t$. This new segment is subjected to strain ε_c and moves at speed $v_c = \dot{a}\varepsilon_c$, and so the rate at which the sum of potential and kinetic energy increases is

$$\begin{aligned} \dot{E}_{pot} + \dot{E}_{kin} &= \left(\tfrac{1}{2} E\varepsilon_c^2 + \tfrac{1}{2}\rho v_c^2\right) bh\dot{a} \\ &= \tfrac{1}{2}(E + \rho\dot{a}^2)\varepsilon_c^2 bh\dot{a} \end{aligned} \tag{36}$$

The important point here is that the potential energy of the bar and interface as well as the kinetic energy of the bar from the current crack tip to infinity remains constant, due to self-similarity. These energy terms would have to be evaluated by integration, but since they do not change in time, their values are not needed.

Formally, the foregoing arguments can be verified by splitting each of the integrals in (13)–(14) into the parts that correspond (i) to the fully delaminated segment, from $x = 0$ to $x = a = a_0 + \dot{a}t$, and (ii) to the cohesive and elastic zone, from $x = a$ to infinity, and by rewriting the integrals in terms of the shifted spatial coordinate $\hat{x}$:

$$\begin{aligned} E_{pot} &= bh \int_0^a \tfrac{1}{2} E u_{,x}^2 \, \mathrm{d}x + bh \int_a^\infty \tfrac{1}{2} E u_{,x}^2 \, \mathrm{d}x \\ &\quad + b \int_0^a \tfrac{1}{2}(1-D) k u^2 \, \mathrm{d}x \\ &\quad + b \int_a^\infty \tfrac{1}{2}(1-D) k u^2 \, \mathrm{d}x \\ &= bha \tfrac{1}{2} E\varepsilon_c^2 + bh \int_0^\infty \tfrac{1}{2} E \hat{u}'^2 \, \mathrm{d}\hat{x} \end{aligned}$$

$$+b\int_0^\infty \tfrac{1}{2}(1-\hat{D})k\hat{u}^2\,\mathrm{d}\hat{x} \tag{37}$$

$$\begin{aligned} E_{kin} &= bh\int_0^a \tfrac{1}{2}\rho u_{,t}^2\,\mathrm{d}x + bh\int_a^\infty \tfrac{1}{2}\rho u_{,t}^2\,\mathrm{d}x \\ &= bha\tfrac{1}{2}\rho\,(-\varepsilon_c\dot{a})^2 \\ &\quad + bh\int_0^\infty \tfrac{1}{2}\rho\dot{a}^2\hat{u}'^2\,\mathrm{d}\hat{x} \end{aligned} \tag{38}$$

The integrals of $(1-\hat{D})\hat{u}^2$ or $\hat{u}'^2$ from zero to infinity are independent of time, and so differentiation of (37)–(38) with respect to time leads to the result already presented in (36). Finally, the rate of the work of fracture can be expressed as

$$\begin{aligned} P_{fra} &= P_{rel} = F_c\times v_c - \dot{E}_{pot} - \dot{E}_{kin} \\ &= Ebh\varepsilon_c^2\dot{a} - \tfrac{1}{2}(E\varepsilon_c^2 + \rho\dot{a}^2\varepsilon_c^2)bh\dot{a} \\ &= \tfrac{1}{2}bh\varepsilon_c^2(E-\rho\dot{a}^2)\dot{a} \end{aligned} \tag{39}$$

Comparing this with (33), we find that the rate-dependent fracture energy is given by

$$G_c = \tfrac{1}{2}h\varepsilon_c^2(E-\rho\dot{a}^2) \tag{40}$$

This formula is easier to manage than (34) because it does not require integration, but ε_c still needs to be computed by solving a boundary value problem and depends on the crack speed.

The evaluation of ε_c is not trivial and in most cases needs to be done numerically. However, some insight into the general relations that link the basic response characteristics is gained if ε_c is expressed in terms of G_c based on (40) and then eliminated from expressions (31) and (32) for the force needed to drive the delamination process, F_c, and the speed of the fully delaminated bar segment, v_c. This leads to

$$\varepsilon_c = \sqrt{\frac{2G_c}{h(E-\rho\dot{a}^2)}} \tag{41}$$

$$F_c = Ebh\varepsilon_c = b\sqrt{\frac{2hEG_c}{1-\dot{a}^2/c^2}} \tag{42}$$

$$v_c = \dot{a}\varepsilon_c = \sqrt{\frac{2G_c\dot{a}^2}{h(E-\rho\dot{a}^2)}} \tag{43}$$

It is also useful to normalize the crack speed, $\dot{a}$, and the bar end speed, v_c, by the speed of elastic waves in the bar, $c=\sqrt{E/\rho}$. In terms of the relative crack speed, $\alpha=\dot{a}/c$, Eqs. (41)–(43) can be presented in the form

$$\varepsilon_c = \sqrt{\frac{2G_c}{hE}}\,\frac{1}{\sqrt{1-\alpha^2}} \tag{44}$$

$$F_c = b\sqrt{2hEG_c}\,\frac{1}{\sqrt{1-\alpha^2}} \tag{45}$$

$$\frac{v_c}{c} = \sqrt{\frac{2G_c}{hE}}\,\frac{\alpha}{\sqrt{1-\alpha^2}} \tag{46}$$

Let us note that the preceding results are in many aspects similar to other examples of self-similar dynamic fracture that can be found in Freund (1998).

4 Reference solutions for rate-independent model

4.1 Global characteristics

For a rate-independent model (and a monotonic process), damage is uniquely linked to the displacement jump by damage law (5), which can be rewritten as $\hat{D}=g(-\hat{u})$ because $[\![u]\!]=-u$ and the difference between u and $\hat{u}$ and between D and $\hat{D}$ is only formal. Consequently, the integral in (34) can be transformed into an integral with $[\![u]\!]$ as the integration variable:

$$G_c = -\int_0^\infty \tfrac{1}{2}k\hat{u}^2\hat{D}'\,\mathrm{d}\hat{x} = \int_0^{u_f}\tfrac{1}{2}k[\![u]\!]^2 g'([\![u]\!])\,\mathrm{d}[\![u]\!] \tag{47}$$

Here, we have taken into account that $\hat{D}'\,\mathrm{d}\hat{x} = \mathrm{d}\hat{D} = (\mathrm{d}g/\mathrm{d}[\![u]\!])\,\mathrm{d}[\![u]\!]$ and we have denoted by g' the derivative of the damage function g with respect to its argument, i.e., to the displacement jump. We have also used the boundary conditions $\hat{u}(\infty)=0$ and $\hat{u}(0)=-u_f$, the latter being the consequence of $\hat{D}(0)=1$ and $g(u_f)=1$. Integration by parts then leads to

$$\begin{aligned} G_c &= \int_0^{u_f}\tfrac{1}{2}k[\![u]\!]^2 g'([\![u]\!])\,\mathrm{d}[\![u]\!] \\ &= \left[\tfrac{1}{2}k[\![u]\!]^2 g([\![u]\!])\right]_{[\![u]\!]=0}^{u_f} \\ &\quad - \int_0^{u_f} k[\![u]\!]g([\![u]\!])\,\mathrm{d}[\![u]\!] \\ &= \int_0^{u_f}(1-g([\![u]\!]))\,k[\![u]\!]\,\mathrm{d}[\![u]\!] = \\ &= \int_0^{u_f}\tau([\![u]\!])\,\mathrm{d}[\![u]\!] \end{aligned} \tag{48}$$

where $\tau([\![u]\!]) = (1-g([\![u]\!]))\,k[\![u]\!]$ is the interfacial shear stress evaluated from constitutive equation (3) combined with damage law (5). This confirms that, for a rate-independent model, the work of separation per unit area of fully delaminated zone is independent of

the crack speed and corresponds to the static fracture energy, G_{c0}, i.e., to the area under the rate-independent cohesive diagram.

For a given rate-independent damage law, the area under the cohesive diagram can be evaluated from parameters of this law and the elastic interface stiffness k, as exemplified by formulae (9)–(10) derived in Sect. 2.1. Conversely, one could consider G_{c0} as one of primary material properties and calibrate the model accordingly.

Substituting $G_c = G_{c0}$ into (41), we find that the axial strain in the fully delaminated zone can be expressed as

$$\varepsilon_c^{(i)} = \sqrt{\frac{2G_{c0}}{hE}} \frac{1}{\sqrt{1-\alpha^2}} = \frac{\varepsilon_{c0}}{\sqrt{1-\alpha^2}} \tag{49}$$

where

$$\varepsilon_{c0} = \sqrt{\frac{2G_{c0}}{hE}} \tag{50}$$

is the value of $\varepsilon_c^{(i)}$ obtained for infinitely slow delamination. Superscript i refers to the rate-independent damage model. Note that G_c in (41) can in general depend on the crack speed, but G_{c0} in formula (49) covering the special case of rate-independent model is a material constant, and so ε_{c0} is a material constant, too. The right-hand side of (49) indicates that the strain in the fully delaminated zone increases in inverse proportion to $\sqrt{1-\alpha^2}$ where $\alpha = \dot{a}/c$ is the relative crack speed.

In a similar way, $G_c = G_{c0}$ can be substituted into (42)–(43), in order to characterize the crack-speed sensitivity of the force that is needed to drive the crack,

$$F_c^{(i)} = b\sqrt{2hEG_{c0}} \frac{1}{\sqrt{1-\alpha^2}} = \frac{F_{c0}}{\sqrt{1-\alpha^2}} \tag{51}$$

and of the relative speed of the fully delaminated zone,

$$\frac{v_c^{(i)}}{c} = \sqrt{\frac{2G_{c0}}{hE}} \frac{\alpha}{\sqrt{1-\alpha^2}} = \frac{\alpha\varepsilon_{c0}}{\sqrt{1-\alpha^2}} \tag{52}$$

For infinitely slow delamination, i.e., under static conditions, the force needed to drive the failure process is

$$F_{c0} = b\sqrt{2hEG_{c0}} \tag{53}$$

This formula was derived already by Kendall (1975), who studied the so-called peeling test and obtained the mode-II delamination test as a special case for peeling angle set to zero; see the Appendix for more details.

The foregoing equations indicate that the sole interfacial parameter governing the conditions of propagation in a dynamic steady process for a rate-independent damage model is G_{c0}, i.e., the area under the cohesive diagram. Under dynamic steady-process conditions, the shape of the diagram plays no role. Another interesting point is that the influence of the relative crack speed α on global characteristics (such as the applied force or bar end speed) is universal, independent of material parameters. The force is proportional to $1/\sqrt{1-\alpha^2}$ and the bar end speed to $\alpha/\sqrt{1-\alpha^2}$. The fracture energy (work of separation per unit area) does not change at all. Of course, all these statements apply exclusively to models with a rate-independent damage law.

4.2 Analytical solution

Even though some of the global characteristics of the failure process can be directly linked to a few geometric and material parameters, the precise distribution of damage or displacement jump along the propagating damage process zone depends on the specific form of the damage law and, in general, would need to be computed numerically. For the rate-independent model with damage functions introduced in Sect. 2.2, it is possible to find analytical solutions, which may serve as a reference and benchmark for numerical methods.

Since the rate-independent formulation directly links the damage variable to the displacement jump, it is possible to eliminate the damage field from (25) and rewrite the governing equation as

$$bh\left(E - \rho\dot{a}^2\right)\hat{u}''(\hat{x}) = bk\left(1 - g(-\hat{u}(\hat{x}))\right)\hat{u}(\hat{x}) \tag{54}$$

As already explained in Sect. 3.1, in the fully delaminated zone where $\hat{x} < 0$, $-\hat{u} > u_f$ and $\hat{D} = g(-\hat{u}) = 1$, equation (54) reduces to (26) and the solution is a linear function (27), with constants u_c and ε_c still to be determined. Now we have to search for the solution of (54) in the damaging and elastic zone where $\hat{x} > 0$, $-\hat{u} < u_f$ and $\hat{D} = g(-\hat{u}) < 1$. We are inter-

ested in the particular solution that satisfies boundary conditions $\hat{u} = -u_f$ at $\hat{x} = 0$ and $\hat{u} \to 0$ as $\hat{x} \to \infty$.

If the crack speed $\dot{a}$ is below the elastic wave speed $c = \sqrt{E/\rho}$, which can be expected to be the typical case, the expression $E - \rho\dot{a}^2$ is positive and equation (54) can be written as

$$l^2\hat{u}''(\hat{x}) = \left(1 - g(-\hat{u}(\hat{x}))\right)\hat{u}(\hat{x}) \tag{55}$$

where

$$l = \sqrt{\frac{h\left(E - \rho\dot{a}^2\right)}{k}} \tag{56}$$

is an auxiliary variable with the dimension of length. In terms of the dimensionless ratio $\alpha = \dot{a}/c$, equation (56) is rephrased as

$$l = l_0\sqrt{1 - \alpha^2} \tag{57}$$

where

$$l_0 = \sqrt{\frac{hE}{k}} \tag{58}$$

is a characteristic length that can be derived from the basic parameters h, E and k. Note that l_0 is a given constant while l depends on the relative crack speed α.

4.2.1 Solution for a damage power law

For the power law (6), the analytical solution developed in Guimard et al. (2009) can be presented in the form

$$\hat{u}(\hat{x}) = \frac{(n+2)u_f}{2}\left(\tanh^2\left(\frac{n\hat{x}}{2l} + \operatorname{atanh}\sqrt{\frac{n}{n+2}}\right) - 1\right) \tag{59}$$

where tanh is the hyperbolic tangent and atanh is its inverse. The corresponding strain at $\hat{x} = 0$ is

$$\begin{aligned}\varepsilon_c^{(i)} &= \hat{u}'(0) = \frac{u_f}{l}\sqrt{\frac{n}{n+2}} \\ &= u_f\sqrt{\frac{nk}{(n+2)h(E - \rho\dot{a}^2)}}\end{aligned} \tag{60}$$

Recall that a general formula (49) for strain $\varepsilon_c^{(i)}$ was developed in Sect. 4.1 based on energy balance arguments. For the present model, the area under the cohesive diagram is given by (9), and one can check that if this expression is substituted for G_{c0}, the general formula (49) indeed yields the same result as the present approach based on an analytical solution of a boundary value problem leading to formula (60).

The power law with $n = 1$ will later be used to check the numerical procedure developed for rate-dependent damage models. This case corresponds to a quadratic stress-displacement relation with $G_{c0} = ku_f^2/6$ and $\varepsilon_c^{(i)} = \sqrt{1/3}\,u_f/l$.

4.2.2 Solution for a linear cohesive law

The linear softening model, described by damage law (7), is one of the most frequently used in the literature. It corresponds to a linear elastic behaviour of the interface up to displacement jump u_p, followed by linear softening with full damage at u_f. The third parameter of the model is the elastic interface stiffness, k. The area under the static stress-displacement diagram is given by (10). A cohesive law of this type is often called "linear" because it has a linear softening branch. Taking into account that the full cohesive diagram consists of two straight segments (linear elasticity and linear softening), we will refer here to a triangular cohesive diagram.

The governing differential equation (55) is written separately in the interval of growing damage and in the interval in which the response remains elastic:

$$l^2\hat{u}''(\hat{x}) = -\frac{u_p}{u_f - u_p}\left(u_f + \hat{u}(\hat{x})\right) \qquad \text{for } \hat{x} \in [0, \hat{x}_e] \tag{61}$$

$$l^2\hat{u}''(\hat{x}) = \hat{u}(\hat{x}) \qquad \text{for } \hat{x} \in [\hat{x}_e, \infty) \tag{62}$$

Here, $\hat{x} = 0$ corresponds to the crack tip, at which $\hat{u} = -u_f$, and $\hat{x}_e$ denotes the point at the boundary between the elastic zone and the damaging zone, at which $\hat{u} = -u_p$. The value of $\hat{x}_e$ is not know a priori and must be determined along with the integration constants from appropriate boundary and continuity conditions.

The general solution of equation (62) reads

$$\hat{u}(\hat{x}) = C_1 e^{\hat{x}/l} + C_2 e^{-\hat{x}/l} \qquad \text{for } \hat{x} \in [\hat{x}_e, \infty) \tag{63}$$

where C_1 and C_2 are integration constants. The solution that we are interested in must satisfy conditions

$$\hat{u}(\hat{x}_e) = -u_p \tag{64}$$

$$\lim_{\hat{x}\to\infty} \hat{u}(\hat{x}) = 0 \tag{65}$$

from which $C_1 = 0$ and $C_2 = -u_p\, \mathrm{e}^{\hat{x}_e/l}$. Constants C_1 and C_2 are eliminated but $\hat{x}_e$ still remains unknown.

The general solution of equation (61) reads

$$\hat{u}(\hat{x}) = -u_f + C_3 \sin\sqrt{\frac{u_p}{u_f-u_p}}\frac{\hat{x}}{l} + C_4 \cos\sqrt{\frac{u_p}{u_f-u_p}}\frac{\hat{x}}{l} \qquad \text{for } \hat{x}\in[0,\hat{x}_e] \tag{66}$$

where C_3 and C_4 are additional integration constants. The solution that we are interested in must satisfy conditions

$$\hat{u}(0) = -u_f \tag{67}$$

$$\hat{u}(\hat{x}_e) = -u_p \tag{68}$$

which imply that $C_4 = 0$ and

$$C_3 = \frac{u_f-u_p}{\sin\sqrt{\frac{u_p}{u_f-u_p}}\frac{\hat{x}_e}{l}} \tag{69}$$

The remaining unknown, $\hat{x}_e$, can now be determined from the condition of continuous differentiability of $\hat{u}(\hat{x})$ (which follows from continuity of normal force in the bar). By matching the derivatives of solutions (63) and (66) at $\hat{x} = \hat{x}_e$, we obtain the equation

$$\sqrt{u_p(u_f-u_p)}\,\mathrm{cotg}\sqrt{\frac{u_p}{u_f-u_p}}\frac{\hat{x}_e}{l} = u_p \tag{70}$$

from which

$$\hat{x}_e = l\sqrt{\frac{u_f-u_p}{u_p}}\arctan\sqrt{\frac{u_f-u_p}{u_p}} \tag{71}$$

Substituting (71) into (69), we get $C_3 = \sqrt{u_f(u_f-u_p)}$. The resulting dimensionless displacement function is thus described by

$$\hat{u}(\hat{x}) = \begin{cases} -u_f + \sqrt{u_f(u_f-u_p)}\sin\sqrt{\frac{u_p}{u_f-u_p}}\frac{\hat{x}}{l} & \text{for } \hat{x}\in[0,\hat{x}_e] \\ -u_p\,\exp\left(-\frac{\hat{x}-\hat{x}_e}{l}\right) & \text{for } \hat{x}\in[\hat{x}_e,\infty) \end{cases} \tag{72}$$

where $\hat{x}_e$ is given by (71). Finally, we can evaluate

$$\varepsilon_c^{(i)} = \hat{u}'(0) = \frac{\sqrt{u_p u_f}}{l} = \sqrt{\frac{k u_p u_f}{h(E-\rho\dot{a}^2)}} \tag{73}$$

Since the area under the triangular stress-displacement diagram is given by (10), one can check again that the strain obtained by solving the boundary value problem and given by formula (73) is the same as what would be obtained from the general formula (49) by substituting G_{c0} according to (10).

5 Bounded-rate damage model

5.1 Formulation of a bounded-rate delayed damage model

In what follows we will consider a specific form of rate dependence but the methodology derived here could be applied to any case of local rate dependence. The principal idea of a **delayed damage model with bounded damage rate** is to consider that the damage process cannot be arbitrarily fast and the damage rate never exceeds a certain limit, which can be expressed as $1/\tau_c$ where τ_c is a characteristic time (considered here as a material property).

A possible way to construct such a model was proposed in Allix and Deü (1997). Based on the damage function $g(\llbracket u\rrbracket)$ determined by a static test, one defines a slightly modified function $g_s(\llbracket u\rrbracket)$ that is equal to the original one as long as $\llbracket u\rrbracket \le u_f$ but exceeds 1 for higher values of the displacement jump $\llbracket u\rrbracket$. For instance, for the power law one can use the expression specified on the first line of (6) even when the displacement jump exceeds u_f, i.e., one defines

$$g_s(\llbracket u\rrbracket) = \left(\frac{\llbracket u\rrbracket}{u_f}\right)^n \tag{74}$$

In the range $\llbracket u\rrbracket > u_f$ where the resulting value of g_s is larger than 1, this value does not represent the

damage anymore, but it can be used for evaluation of a generalized damage-driving force. According to the delayed damage model, damage is supposed to grow only if $g_s([\![u]\!])$ exceeds the current damage, D, and the damage rate increases with increasing difference $g_s([\![u]\!]) - D$.

In the simplest case, the rate form of the damage law could assume proportionality between the rate of damage and the "driving force", but then there would be no bound on the rate and damage could, in principle, grow arbitrarily fast. A bounded-rate version of the delayed damage model (Allix and Deü 1997) postulates the evolution law

$$D_{,t} = \begin{cases} \dfrac{1}{\tau_c}\left(1 - \mathrm{e}^{-A_c\langle g_s([\![u]\!]) - D\rangle}\right) & \text{if } D < 1 \\ 0 & \text{if } D = 1 \end{cases} \tag{75}$$

where Macauley brackets $\langle \ldots \rangle$ denote the positive part (i.e., $\langle x\rangle = x$ if $x \geq 0$ and $\langle x\rangle = 0$ if $x < 0$) and τ_c and A_c are nonnegative parameters. Parameter τ_c has the dimension of time, and its reciprocal value is the maximum possible damage rate, which explains why we refer to a bounded-rate damage model.

If $g_s([\![u]\!]) \leq D$, the positive part of $g_s([\![u]\!]) - D$ is zero and the formula on the first line of (75) gives zero damage rate. If $g_s([\![u]\!])$ is only slightly larger than D, the formula leads to a very low damage rate. In the limit, for infinitely slow increase of the displacement jump, the behavior predicted by the rate-independent model with $D = g([\![u]\!])$ is recovered. On the other hand, for very fast loading, the damage rate increases but never exceeds $1/\tau_c$. Since the damage growth is delayed as compared to the response of the rate-independent model with the same applied displacement jump evolution, higher stresses are generated by the rate-dependent model. The value of function g_s can exceed 1, and then the formula on the first line of (75) would predict further growth of damage even if D is already equal to 1 and the damage is complete. This is taken care of by the condition that the formula should be used only as long as $D < 1$ and when the damage variable becomes equal to 1, its further evolution is stopped; see the second line of (75).

In some studies dealing with delayed damage models, damage was assumed to be driven by the difference $g([\![u]\!]) - D$, or, for continuum damage models, by $g(\kappa) - D$ where κ is the maximum previously reached equivalent strain; see, e.g., Desmorat et al. (2010). Here, g is the original damage function for the rate-independent version of the model, which is always bounded by 1. For high rates, this induces a longer delay of the damage than the presently considered formulation with an unbounded driving force related to the extended damage function g_s. In fact, for a formulation based on g, the value $D = 1$ is never reached at a finite time. A critical value slightly smaller than 1 has thus to be selected for the definition of a fully damaged material.

Faster propagation of damage during the terminal stage can be achieved by replacing the original damage function g by a suitably modified function g_s, as already described. However, the definition of function g_s in the range where $g = 1$ may appear quite artificial and to a certain extent arbitrary. Moreover, there exist softening models with a long tail that approaches zero stress only asymptotically (not at a finite value of displacement jump), which means that function g remains smaller than 1 for all values of $[\![u]\!]$. It is then impossible to define g_s different from g while preserving the behavior of the original rate-independent model in the limit of infinitely slow damage growth.

It may thus be helpful to consider a newly proposed type of damage evolution law, which is inspired by a re-interpretation of formula (75) in the special case of g_s given by the power law (74) with exponent $n = 1$. In this case, the argument of the exponential function in (75) can be rewritten as

$$\begin{aligned} -A_c\left\langle \frac{[\![u]\!]}{u_f} - D\right\rangle &= -\frac{A_c}{u_f}\left\langle [\![u]\!] - u_f D\right\rangle \\ &= -A_c^*\left\langle [\![u]\!] - g^*(D)\right\rangle \end{aligned} \tag{76}$$

where $A_c^* = A_c/u_f$ is a transformed parameter and g^* denotes the inverse function of the extended damage function g_s, defined here by $g^*(D) = u_f D$. Consequently, a damage evolution law postulated in the form

$$D_{,t} = \begin{cases} \dfrac{1}{\tau_c}\left(1 - \mathrm{e}^{-A_c^*\langle [\![u]\!] - g^*(D)\rangle}\right) & \text{if } D < 1 \\ 0 & \text{if } D = 1 \end{cases} \tag{77}$$

is, in the present special case, fully equivalent to the original law (75).

Graphically, the difference between (75) and (77) is illustrated in Fig. 3a. The dashed line corresponds to the rate-independent damage law (i.e., to $D = g([\![u]\!])$),

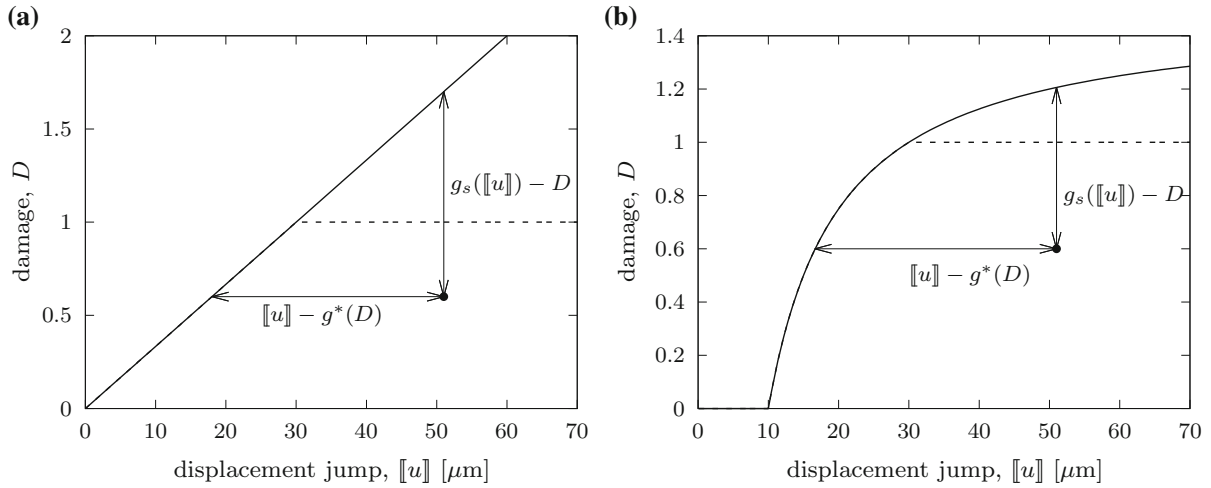

Fig. 3 Graphical interpretation of the damage-driving terms in Eqs. (75) and (77): dependence of damage on displacement jump in rate-independent case given by a **a** linear function, **b** nonlinear function

the solid line to the graph of the extended damage function g_s, and the point marked by a filled circle to the current combination of displacement jump and damage attained by a delayed damage model. According to the original law (75), the damage rate is evaluated from the difference $g_s([\![u]\!]) - D$, which corresponds to the vertical distance of the "current state point" from the inclined solid line, and according to the modified law (77), the damage rate is evaluated from the difference $[\![u]\!] - g^*(D)$, which corresponds to the horizontal distance of the same point from the same line. Since the line is straight and has slope $1/u_f$, the vertical distance multiplied by parameter A_c gives the same result as the horizontal distance multiplied by an adjusted parameter A_c^* equal to A_c/u_f.

The foregoing considerations look trivial, but the important point is that even though g^* has been introduced as the inverse function of the "extended damage function" g_s, we only need to evaluate $g^*(D)$ for $D < 1$. Consequently, it is sufficient to invert the original damage function g and there is no need to construct its artificial extension to g_s. In graphical terms, the vertical distance in Fig. 3a depends on the shape of the extended diagram above $D = 1$ while the horizontal distance always uses just the original part of the diagram below $D = 1$. Therefore, the modified law written in its general format (77) can be applied to models with any type of rate-independent damage function g in a straightforward way, without the need for an artificial extension from g to g_s. It is sufficient to construct function g^* by inversion of g in the range where g is a strictly increasing function, which corresponds to the range where $0 < D < 1$. The values of g^* at 0 and 1 are then defined by continuous extension.

The rigorous transformation presented in (76) applies only to the special case of linear function g_s. In this case, formulations based on (75) and (77) are fully equivalent. For nonlinear functions, the replacement of (75) by (77) leads to a different model, as indicated graphically in Fig. 3b. Here, the horizontal distance is not proportional to the vertical distance, and the modified model does not exhibit the same behavior as the original one. Still, it is ensured that if the displacement jump increases very fast, the "driving force" (horizontal distance) can be large even if the damage variable is already close to 1.

For illustration, for the power law (6) the inverse function is given by

$$g^*(D) = u_f D^{1/n} \tag{78}$$

and for the law (7) that corresponds to linear softening, it is given by

$$g^*(D) = \frac{u_p u_f}{u_f - (u_f - u_p)D} \tag{79}$$

Physically, $g^*(D)$ corresponds to the displacement jump that would induce damage D under static loading. The value of g^* at $D = 0$ is the damage threshold,

equal to 0 for the power law (because damage starts growing right at the onset of loading) and to u_p for the law leading to linear softening. For both laws, $g^*(1) = u_f$.

5.2 Transformation to dimensionless variables

Let us return to the problem of self-similar dynamic delamination. Recall that the equation of motion combined with the assumed form of the solution valid for the dynamic steady process resulted into Eq. (25). In the rate-independent case, the damage variable was eliminated by substituting the damage law, and a second-order ordinary differential equation (54) was obtained in Sect. 4.2. For the rate-dependent damage model, Eq. (25) needs to be solved simultaneously with the damage evolution Eq. (77), which has the character of a first-order differential equation. Since an analytical solution is not available for the rate-dependent case, the problem will be solved numerically.

To simplify the description and to reduce the number of parameters, it is useful to convert the displacement and the spatial coordinate into dimensionless variables. The dimensionless displacement is defined here as $\tilde{u} = -\hat{u}/u_f$, because then $\tilde{u} = 1$ corresponds to the state at complete damage (when the displacement jump $[\![u]\!] = -\hat{u}$ attains the critical value u_f). On the other hand, the spatial coordinate is normalized by the length parameter l introduced in (56), because then the coefficient l^2 multiplying the term with the second derivative in the governing equation will be replaced by 1. Therefore, the dimensionless coordinate is defined as $\tilde{x} = \hat{x}/l$. In rigorous notation, we will denote by $\tilde{D}$ the damage variable considered as a function of the dimensionless coordinate $\tilde{x}$, which means that $\hat{D}(\hat{x}) = \tilde{D}(\hat{x}/l)$.

Since

$$\hat{u}(\hat{x}) = -u_f \tilde{u}(\hat{x}/l) \tag{80}$$

$$\frac{\mathrm{d}\hat{u}(\hat{x})}{\mathrm{d}\hat{x}} = -u_f \frac{\mathrm{d}\tilde{u}(\hat{x}/l)}{\mathrm{d}\tilde{x}} \frac{\mathrm{d}\tilde{x}}{\mathrm{d}\hat{x}} = -\frac{u_f}{l} \frac{\mathrm{d}\tilde{u}(\hat{x}/l)}{\mathrm{d}\tilde{x}} \tag{81}$$

$$\frac{\mathrm{d}^2\hat{u}(\hat{x})}{\mathrm{d}\hat{x}^2} = -\frac{u_f}{l^2} \frac{\mathrm{d}^2\tilde{u}(\hat{x}/l)}{\mathrm{d}\tilde{x}^2} \tag{82}$$

and since l is defined such that $h(E-\rho\dot{a}^2)/kl^2 = 1$, Eq. (25) rewritten in terms of the dimensionless variables reduces to

$$\tilde{u}''(\tilde{x}) = \left(1 - \tilde{D}(\tilde{x})\right) \tilde{u}(\tilde{x}) \tag{83}$$

For convenience, we use again primes for derivatives, this time with respect to $\tilde{x}$.

In the following analyses, the bounded-rate delayed damage model will be used in its newly proposed form (77). In the interval in which damage grows monotonically and remains smaller than 1, we can use the first line on the right-hand side of (77) and drop the Macauley brackets. Taking into account that

$$D, t = \frac{\partial D}{\partial t} = \frac{\mathrm{d}\tilde{D}}{\mathrm{d}\tilde{x}} \frac{\mathrm{d}\tilde{x}}{\mathrm{d}\hat{x}} \frac{\partial \hat{x}}{\partial t} = \tilde{D}' \frac{1}{l}(-\dot{a}) = -\frac{\dot{a}}{l}\tilde{D}' \tag{84}$$

we can rewrite the damage evolution equation (77) in the partially damaged region as

$$\tilde{D}' = -\frac{l}{\dot{a}\tau_c}\left(1 - \mathrm{e}^{-A_c(\tilde{u} - \tilde{g}^*(\tilde{D}))}\right) \tag{85}$$

where $\tilde{g}^*$ is the inverse function of the dimensionless function $\tilde{g}$ defined by $\tilde{g}(\tilde{u}) = g(u_f\tilde{u})$, which leads to $\tilde{g}^*(D) = g^*(D)/u_f$. For the model with a parabolic cohesive diagram, described by the damage law (6) and inverse damage function (78) with $n = 1$, the corresponding dimensionless inverse damage function has the form

$$\tilde{g}^*(\tilde{D}) = \tilde{D} \tag{86}$$

Note that in (85) we have returned back to the original parameter A_c, which was hidden in (77) in the form of a transformed parameter $A_c^* = A_c/u_f$, introduced just for simplicity. After conversion to the dimensionless form, it is more convenient to use A_c, which is dimensionless and its value can be directly compared to what was originally used in (75).

For further analysis, it is convenient to introduce a dimensionless parameter

$$\lambda = \frac{l}{\dot{a}\tau_c} = \frac{l_0}{c\alpha\tau_c}\sqrt{1-\alpha^2} = \lambda_0\sqrt{\frac{1}{\alpha^2} - 1} \tag{87}$$

where $\lambda_0 = l_0/(c\tau_c)$ is a dimensionless material parameter and $\alpha = \dot{a}/c$ is the relative crack speed. The final form of the dimensionless differential equation derived from the rate-dependent damage law (77) is

$$\tilde{D}'(\tilde{x}) = -\lambda\left(1 - \mathrm{e}^{-A_c(\tilde{u}(\tilde{x}) - \tilde{g}^*(\tilde{D}(\tilde{x})))}\right) \tag{88}$$

Note that (88) is applicable only in the damage process zone (zone of incomplete damage), represented here by the interval $(0, \infty)$. In the fully delaminated zone, i.e., for $\tilde{x} < 0$, it has to be replaced by $\tilde{D}'(\tilde{x}) = 0$.

Eqs. (88) and (83) represent a set of two differential equations, one of the first order and the other of the second order, for two unknown functions, $\tilde{u}$ and $\tilde{D}$. They have to be solved on $[0, \infty)$ with boundary conditions

$$\tilde{D}(0) = 1 \tag{89}$$

$$\lim_{\tilde{x}\to\infty} \tilde{u}(\tilde{x}) = 0 \tag{90}$$

$$\lim_{\tilde{x}\to\infty} \tilde{D}(\tilde{x}) = 0 \tag{91}$$

The solution depends on dimensionless parameters λ and A_c.

6 Numerical algorithm: the direct shooting method

In general, an approximate solution of Eqs. (83) and (88) has to be constructed numerically. These second- and first-order nonlinear differential equations are solved on the semi-infinite interval $[0, \infty)$ and their solution should satisfy one boundary condition at $\tilde{x} = 0$ and two conditions at $\tilde{x} \to \infty$. It will be shown that the solution can be found efficiently by an adapted version of the shooting method. The main idea of this method is that a boundary value problem is transformed into an initial value problem by adding one or more artificial initial conditions, and the values imposed by the added conditions are then iteratively modified until the solution obtained by numerical integration satisfies the boundary condition(s) on the other end of the interval.

In the present case, one might start at $\tilde{x} = 0$, impose the "true" condition $\tilde{D}(0) = 1$ and two artificial conditions $\tilde{u}(0) = \bar{u}_0$ and $\tilde{u}'(0) = \bar{u}'_0$, and then look for values of $\bar{u}_0$ and $\bar{u}'_0$ for which the numerically integrated solution tends to zero as $\tilde{x}$ approaches infinity. However, for a general choice of $\bar{u}_0$ and $\bar{u}'_0$, the numerical solution would become unbounded and it would be impossible to define real-valued functions of $\bar{u}_0$ and $\bar{u}'_0$ that represent the limits of $\tilde{D}$ and $\tilde{u}$ at infinity. It is therefore much better to perform the numerical integration in the opposite direction. Of course, the procedure cannot really start from $\tilde{x} = \infty$ with values of $\tilde{D}$ and $\tilde{u}$ set to zero, but it can start from a point that is sufficiently far from the origin, with assigned initial values which correspond to the asymptotic form of the solution that approaches zero as $\tilde{x} =\!\!\rightarrow \infty$.

The numerical integration will start at a point $\tilde{x} = \tilde{x}_s$ that is sufficiently far from the origin, such that $\tilde{D}(\tilde{x}_s) \ll 1$. For $\tilde{x} \geq \tilde{x}_s$, the effect of damage is negligible and Eq. (83) can approximately be replaced by

$$\tilde{u}''(\tilde{x}) = \tilde{u}(\tilde{x}) \tag{92}$$

The solution of this linear differential equation that vanishes at plus infinity is

$$\tilde{u}(\tilde{x}) = \tilde{u}_s \mathrm{e}^{-(\tilde{x}-\tilde{x}_s)} \qquad \text{for } \tilde{x} \geq \tilde{x}_s \tag{93}$$

where $\tilde{u}_s$ is the value of $\tilde{u}$ at $\tilde{x} = \tilde{x}_s$. Note that $\tilde{u}'(\tilde{x}) = -\tilde{u}_s \mathrm{e}^{-(\tilde{x}-\tilde{x}_s)}$, and so $\tilde{u}'(\tilde{x}_s) = -\tilde{u}_s$. We still have to find the corresponding asymptotic form of the damage field. To keep the presentation as simple as possible, we consider here function $\tilde{g}^*$ given by (86), which corresponds to the power damage law (6) with exponent $n = 1$. Generalization to other forms of function $\tilde{g}^*$ would be straightforward. Since both $\tilde{u}$ and $\tilde{D}$ are assumed to be small for $\tilde{x} \geq \tilde{x}_s$, we can use the approximation

$$\mathrm{e}^{-A_c(\tilde{u}(\tilde{x})-\tilde{D}(\tilde{x}))} \approx 1 - A_c(\tilde{u}(\tilde{x}) - \tilde{D}(\tilde{x})) \tag{94}$$

and replace (88) by

$$\tilde{D}'(\tilde{x}) = -\lambda A_c(\tilde{u}(\tilde{x}) - \tilde{D}(\tilde{x})) \tag{95}$$

Substituting from (93), we obtain

$$\tilde{D}'(\tilde{x}) - \lambda A_c \tilde{D}(\tilde{x}) = -\lambda A_c \tilde{u}_s \mathrm{e}^{-(\tilde{x}-\tilde{x}_s)} \tag{96}$$

This is a non-homogeneous linear differential equation, which has a general solution

$$\tilde{D}(\tilde{x}) = \frac{\lambda A_c}{1 + \lambda A_c} \tilde{u}_s \mathrm{e}^{-(\tilde{x}-\tilde{x}_s)} + C\mathrm{e}^{\tilde{x}} \tag{97}$$

where C is an arbitrary integration constant. To satisfy condition (91), we set $C = 0$ and evaluate

$$\tilde{D}_s = \tilde{D}(\tilde{x}_s) = \frac{\lambda A_c}{1 + \lambda A_c} \tilde{u}_s \tag{98}$$

Based on the derived form of the asymptotic solution, the shooting method can start from point $\tilde{x}_s$ instead

of from infinity. If we select a suitable value of $\tilde{u}_s$, we can impose "initial" conditions

$$\tilde{u}(\tilde{x}_s) = \tilde{u}_s \tag{99}$$

$$\tilde{u}'(\tilde{x}_s) = -\tilde{u}_s \tag{100}$$

$$\tilde{D}(\tilde{x}_s) = \frac{\lambda A_c \tilde{u}_s}{1 + \lambda A_c} \tag{101}$$

and then integrate numerically Eqs. (88) and (83) **backwards**, i.e., with decreasing $\tilde{x}$. In principle we should find $\tilde{x}_s$ and $\tilde{u}_s$ such that the numerical solution would satisfy the condition $\tilde{D}(0) = 1$, which is the only boundary condition that has not been taken into account yet. However, since the governing differential equations are autonomous (i.e., do not depend explicitly on the independent variable $\tilde{x}$), it is not even necessary to iterate on $\tilde{u}_s$ or on $\tilde{x}_s$. It suffices to select an arbitrary $\tilde{x}_s$ and an arbitrary (but sufficiently small) $\tilde{u}_s$, perform numerical integration and find the point $\tilde{x} = \tilde{x}_D$ at which $\tilde{D}(\tilde{x}_D) = 1$. After that, the already computed solution is simply shifted in space by $\tilde{x}_D$ to the left, such that the point at which $\tilde{D} = 1$ gets to the origin and conditions (99)–(101) are actually valid at $\tilde{x} = \tilde{x}_s - \tilde{x}_D$. The only restriction is that the initial value $\tilde{u}_s$ must be sufficiently small. In fact, it is better to first select $\tilde{D}_s$ sufficiently small, e.g., $\tilde{D}_s = 10^{-4}$, and then compute from (98) the corresponding

$$\tilde{u}_s = \left(1 + \frac{1}{\lambda A_c}\right) \tilde{D}_s \tag{102}$$

To avoid the need for selecting an arbitrary value of $\tilde{x}_s$, and also for stepping in space in the negative direction, it is useful to introduce a transformed spatial variable $\xi = \tilde{x}_s - \tilde{x}$. The spatial fields are then considered as functions of ξ, the initial conditions are imposed at $\xi = 0$, coordinate ξ is incremented and the values of $\tilde{u}$ and $\tilde{D}$ updated. For the purpose of numerical solution, Eqs. (88) and (83) are rewritten as

$$\tilde{D}'(\xi) = \lambda \left(1 - \mathrm{e}^{-A_c(\tilde{u}(\xi) - \tilde{D}(\xi))}\right) \tag{103}$$

$$\tilde{u}''(\xi) = \left(1 - \tilde{D}(\xi)\right) \tilde{u}(\xi) \tag{104}$$

Note the change of sign on the right-hand side of (103) as compared to (88), which is caused by the fact that the primes now denote derivatives with respect to ξ, and $\mathrm{d}/\mathrm{d}\xi = -\mathrm{d}/\mathrm{d}\tilde{x}$. No change of sign is needed for the second derivative in (104).

The finite difference approximation is based on the forward Euler scheme for (103) and on the central difference scheme for (104). In a typical step number k, the equations are approximated by

$$\frac{\tilde{D}_{k+1} - \tilde{D}_k}{\Delta\xi} = \lambda \left(1 - \mathrm{e}^{-A_c(\tilde{u}_k - \tilde{D}_k)}\right) \tag{105}$$

$$\frac{\tilde{u}_{k+1} - 2\tilde{u}_k + \tilde{u}_{k-1}}{(\Delta\xi)^2} = (1 - \tilde{D}_k)\, \tilde{u}_k \tag{106}$$

where $\Delta\xi$ is the step size, and $\tilde{u}_k$ and $\tilde{D}_k$ are the approximate values of $\tilde{D}(\xi_k)$ and $\tilde{u}(\xi_k)$, with $\xi_k = k\,\Delta\xi$, $k = 0, 1, 2, \ldots$. To initialize, the value of $\tilde{D}_0$ is directly set to the selected small value $\tilde{D}_s$, and the value of $\tilde{u}_0$ is set to $\tilde{u}_s$ given by (102). For the first step, we also need the value of $\tilde{u}_{-1}$, which is evaluated from the same asymptotic approximation (93) as $\tilde{u}_0$, leading to

$$\tilde{u}_{-1} = \tilde{u}_s\, \mathrm{e}^{-\Delta\xi} \tag{107}$$

After initialisation, the values of damage and displacement are computed using the recursive formulae

$$\tilde{D}_{k+1} = \tilde{D}_k + \lambda\, \Delta\xi \left(1 - \mathrm{e}^{-A_c(\tilde{u}_k - \tilde{D}_k)}\right) \tag{108}$$

$$\tilde{u}_{k+1} = 2\tilde{u}_k - \tilde{u}_{k-1} + (\Delta\xi)^2 (1 - \tilde{D}_k)\, \tilde{u}_k, \qquad k = 0, 1, 2, 3, \ldots \tag{109}$$

The simulation is terminated when $\tilde{D}_{k+1}$ exceeds 1. Then, the point ξ_D at which $\tilde{D} = 1$ is estimated from the condition

$$\tilde{D}_k + (\xi_D - \xi_k)\lambda \left(1 - \mathrm{e}^{-A_c(\tilde{u}_k - \tilde{D}_k)}\right) = 1 \tag{110}$$

which yields

$$\xi_D = \xi_k + \frac{1 - \tilde{D}_k}{\lambda \left(1 - \mathrm{e}^{-A_c(\tilde{u}_k - \tilde{D}_k)}\right)} \tag{111}$$

Now we can set $\tilde{x} = \xi_D - \xi$ and plot the computed solution as function of the original dimensionless coordinate, $\tilde{x}$, or of the distance from the crack tip, $\hat{x} = l\tilde{x}$.

For simplicity, the foregoing numerical scheme has been developed for a specific form of function $\tilde{g}^*$, given by (86). To cover the general case, it is sufficient to replace everywhere the term $\mathrm{e}^{-A_c(\tilde{u}_k - \tilde{D}_k)}$ by $\mathrm{e}^{-A_c(\tilde{u}_k - \tilde{g}^*(\tilde{D}_k))}$, in particular in formulae (105) and (111), and at the same time to adjust formula (102) for the initial value of displacement. Determination of the asymptotic behavior for $\tilde{x} \to \infty$ depends on the initial part of cohesive diagram. If nonzero damage occurs

for an arbitrarily small displacement jump (which is the case for the power law (6)), the term $\tilde{D}(\tilde{x})$ in the linearized expression on the right-hand side of (94) needs to be replaced by $\tilde{g}_0^{*\prime}\tilde{D}(\tilde{x})$ where $\tilde{g}_0^{*\prime}$ is the derivative of $\tilde{g}^*$ evaluated at $\tilde{D}=0$ (note that, for the model with a parabolic cohesive diagram, $\tilde{g}_0^{*\prime}=1$). When this is taken into account in the derivation, the resulting formula (102) is generalized to

$$\tilde{u}_s = \left(\tilde{g}_0^{*\prime} + \frac{1}{\lambda A_c}\right)\tilde{D}_s \tag{112}$$

On the other hand, if damage remains equal to zero for all displacement jumps below a threshold value u_p (which is the case for the model with a triangular cohesive diagram), equation (88) or (95) should actually be replaced by $\tilde{D}'(\tilde{x})=0$ in the elastic zone characterized by $\tilde{u}(\tilde{x}) \le u_p/u_f$. We can then select point $\tilde{x}_s$ such that $\tilde{u}(\tilde{x}_s)=u_p/u_f$ and the asymptotic displacement field given by (93) is exact. The numerical scheme is initialized by setting $\tilde{u}_s = u_p/u_f$ and $\tilde{D}_s = 0$.

7 Reference example and comparison with FE solution from the literature

7.1 Reference set of material parameters

In the first calculation illustrating the numerical procedure developed in the preceding section, the values of primary material parameters listed in Table 1a are considered, giving rise to the derived parameters evaluated in Table 1b. To evaluate parameter u_f from the initial interface stiffness k and static fracture energy G_{c0}, it is necessary to specify the shape of the cohesive curve considered in the example. A power damage law (6) with $n=1$ is used here, which means that relation (9) can be rewritten as $G_{c0} = ku_f^2/6$, leading to $u_f = \sqrt{6G_{c0}/k}$. Recall that the corresponding dimensionless inverse damage function $\tilde{g}^*$ has the form (86).

7.2 Integration parameters and numerical accuracy

For each given value of the relative crack speed α, we determine λ from (87), combine it with the given value of $A_c=3$, and numerically solve the problem consisting of equations (83) and (88) with boundary conditions (89)–(91) using the shooting method described in Sect. 6. In this way, we obtain the dimensionless displacement $\tilde{u}$ and damage $\tilde{D}$ as functions of the dimensionless coordinate $\tilde{x}$, and we can evaluate the normalized strain at the crack tip, $\tilde{\varepsilon}_c = -\tilde{u}'(0)$, which is then easily transformed into the actual strain at the crack tip,

$$\varepsilon_c = \frac{\mathrm{d}\hat{u}(0)}{\mathrm{d}\hat{x}} = -u_f\frac{\mathrm{d}\tilde{u}(0)}{\mathrm{d}\tilde{x}}\frac{\mathrm{d}\tilde{x}}{\mathrm{d}\hat{x}} = -\frac{u_f}{l}\tilde{u}'(0) = \frac{u_f}{l}\tilde{\varepsilon}_c \tag{113}$$

Finally, the axial force in the fully delaminated part is obtained from (31), the velocity of the fully delaminated part from (32), and the rate-dependent fracture energy from (40).

Consider a crack propagating at 10% of the elastic wave speed. For $\dot{a}=0.1c$ we get $\alpha=0.1$, $\lambda = \lambda_0\sqrt{1/\alpha^2-1} = 0.1\sqrt{100-1} \approx 0.995$ and $l = l_0\sqrt{1-\alpha^2} = 0.995\,l_0 = 4.83\times10^{-3}$ m. For $\lambda=0.995$ and $A_c=3$, the initial value of displacement according to (102) is

$$\begin{aligned}\tilde{u}_s &= \left(1+\frac{1}{\lambda A_c}\right)\tilde{D}_s \\ &= \left(1+\frac{1}{0.995\times 3}\right)\tilde{D}_s \approx 1.335\tilde{D}_s\end{aligned} \tag{114}$$

We select for instance $\Delta\xi = 10^{-4}$ and $\tilde{D}_s = 10^{-3}$, and then we set $\tilde{D}_0 = \tilde{D}_s = 10^{-3}$, $\tilde{u}_0 = \tilde{u}_s = 1.335\,\tilde{D}_s = 1.335\times10^{-3}$ and $\tilde{u}_{-1} = \tilde{u}_s\,\mathrm{e}^{-\Delta\xi} = 1.33488\times10^{-3}$ as initial values for the finite difference scheme described in (108)–(109). After 73,727 steps, the damage at $\xi_{k+1}=7.3727$ is found to be 1.000045 while the damage at $\xi_k = 7.3726$ was 0.999982. By using formula (111), or simply by linear interpolation, we obtain $\xi_D = 7.372628$. The numerical solution plotted as a function of the auxiliary coordinate ξ is shown in Fig. 4. To check that the results are really accurate, the solution has been rerun with a larger step $\Delta\xi = 10^{-3}$. When the new curves would be plotted into Fig. 4, they could not be visually distinguished from the original ones.

A finite difference formula applied to the displacement values $\tilde{u}_k = 1.3324555$ at ξ_k and $\tilde{u}_{k+1} = 1.3325331$ at ξ_{k+1} leads to $\mathrm{d}\tilde{u}/\mathrm{d}\xi \approx (\tilde{u}_{k+1}-\tilde{u}_k)/\Delta\xi = 0.776$ (in higher precision, 0.7762). This is the quantity that has been denoted as $\tilde{\varepsilon}_c$ and corresponds to the negative derivative of $\tilde{u}$ with respect to $\tilde{x}$ at the crack tip. The computed values of $\tilde{\varepsilon}_c$ for various combinations of numerical parameters are listed in Table 2. It turns out that the accuracy achieved with $\tilde{D}_s = 10^{-2}$ and $\Delta\xi = 10^{-3}$ is sufficient.

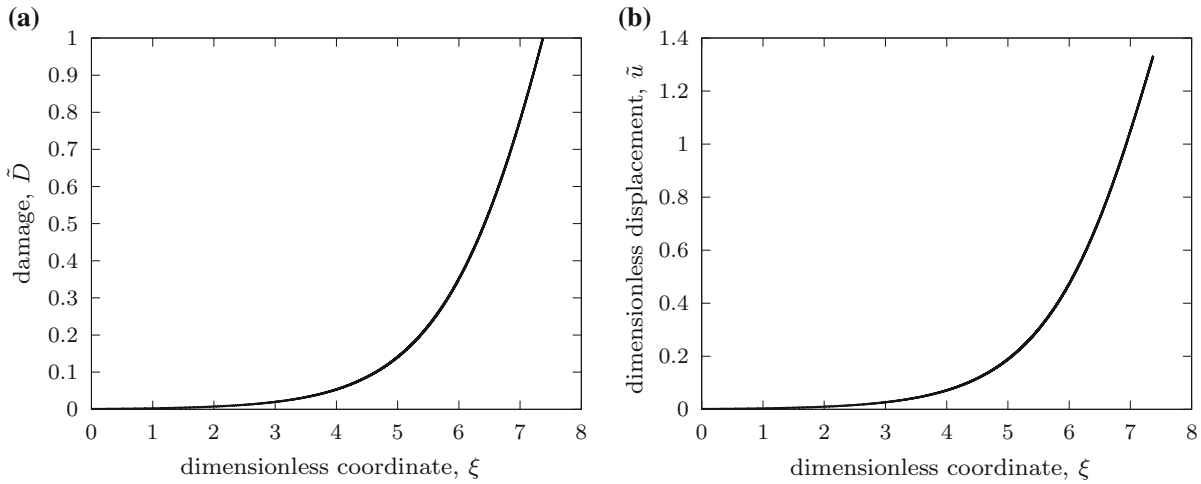

Fig. 4 Reference case, crack speed $\dot{a} = 0.1\,c$: **a** damage and **b** dimensionless displacement obtained by the shooting method with spatial step $\Delta\xi = 0.0001$, starting from initial damage $\tilde{D}_s = 0.001$ at $\xi = 0$ and reaching complete damage $\tilde{D} = 1$ at $\xi = \xi_D = 7.372628$

Table 2 Reference case—accuracy of the numerical solution

Initial damage $\tilde{D}_s$	Spatial step $\Delta\xi$	Normalized strain $\tilde{\varepsilon}_0$
10^{-3}	10^{-4}	0.77619629
10^{-3}	10^{-3}	0.77626748
10^{-3}	10^{-2}	0.77698393
10^{-2}	10^{-4}	0.77619793
10^{-2}	10^{-3}	0.77626914
10^{-2}	10^{-2}	0.77698610

From the computed normalized strain $\tilde{\varepsilon}_c = 0.7762$, all the relevant physical quantities can be evaluated. The actual strain in the fully delaminated part obtained from (113) is $\varepsilon_c = \tilde{\varepsilon}_c u_f/l = 4.822 \cdot 10^{-3}$, the force per unit width applied at the end of the bar is according to (42) given by $F_c/b = Eh\varepsilon_c = 1.136 \cdot 10^6$ N/m, and the speed at which the bar end moves is obtained from (43) as $v_c = \dot{a}\varepsilon_c = 4.684$ m/s. The dynamic fracture energy can be expressed from (40) as $G_c = \frac{1}{2}Eh\varepsilon_c^2(1-\alpha^2) = 2711$ J/m^2.

The numerical solution presented in Fig. 4 can be replotted in terms of the physical coordinate $\hat{x} = l\tilde{x}$, which represents the distance from the crack tip, with the dimensionless displacement $\tilde{u}$ transformed into the real displacement $\hat{u} = -u_f\tilde{u}$; see Fig. 5a, b. For comparison, the dashed curve in Fig. 5a indicates the level of damage that would be obtained for the same displacement jump if the model was considered as rate-independent, i.e., without a delay in damage evolution. The difference between the solid and dashed curves is due to the delay of damage. It is also instructive to look at the distribution of stresses. The shear stress on the damaging interface is plotted in Fig. 5c and the normal stress in the elastic bar in Fig. 5d. Again, the dashed curve in Fig. 5c corresponds to the shear stress that would be produced by the same displacement jump if the model was considered as rate-independent. In that case, the peak value of shear stress, obtained at displacement jump $[\![u]\!] = u_f/2 = 0.015$ mm, would be $\tau_{\max,0} = ku_f/4 = 75$ MPa, and the shear stress would vanish at points where the displacement jump exceeds $u_f = 0.03$ mm. The additional shear stress transmitted by the interface is rate-dependent and originates from the delay of damage. Note that the shear stresses evaluated using the rate-independent model are fictitious and are shown here just to get an idea about the rate effect. These stresses do not satisfy the equations of motion and if the model was really rate-independent, the distribution of displacement jump along the damage process zone would need to be recomputed.

7.3 Effects of inertia and rate dependence

The calculation presented in the previous subsection refers to dynamic delamination of an interface described by a rate-dependent damage model. It is

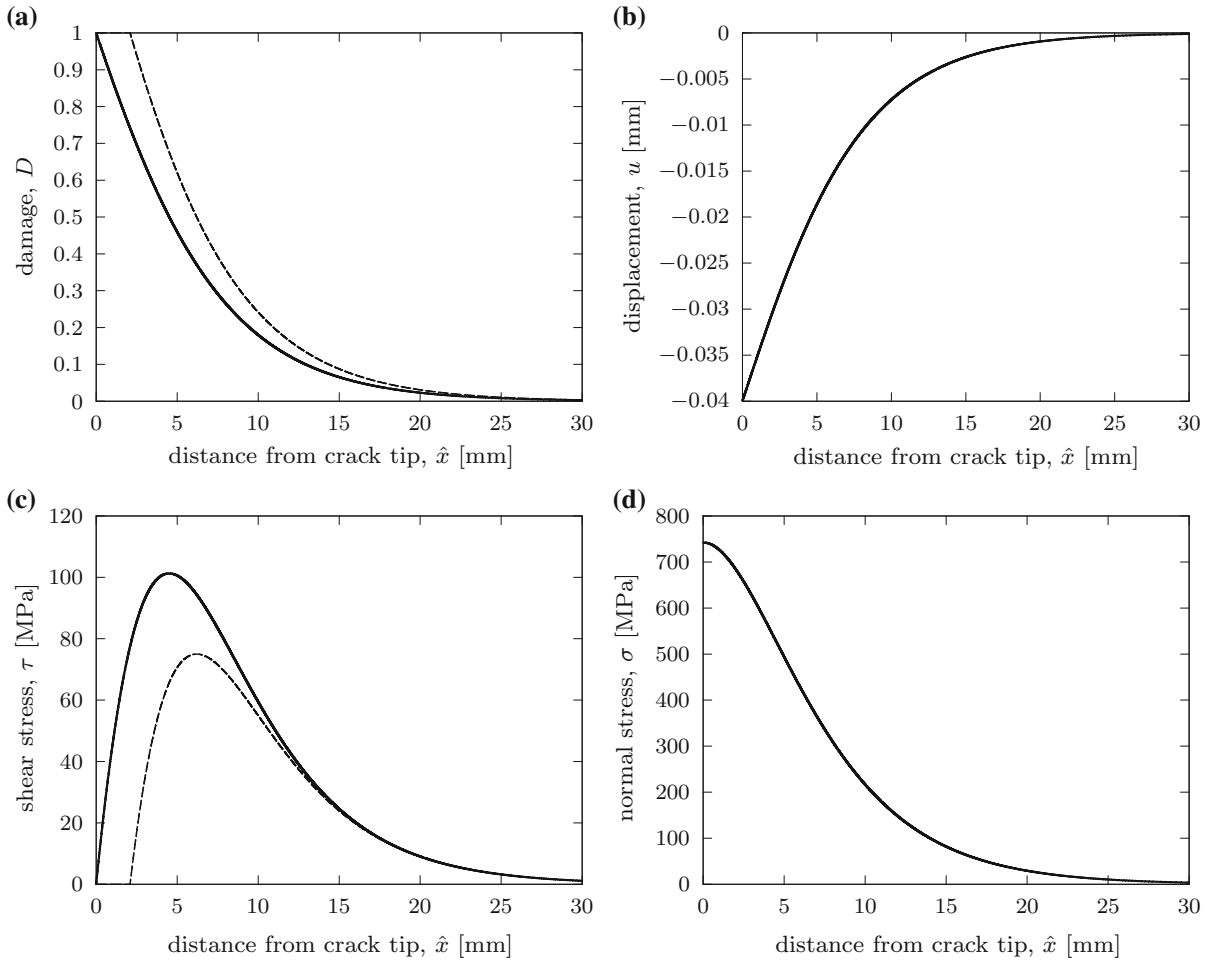

Fig. 5 Reference case, crack speed $\dot{a} = 0.1\,c$: spatial distribution of **a** damage, **b** displacement, **c** shear stress on the interface and **d** normal stress in the bar; dashed curves in **a** and **c** represent values that would be obtained for the same displacement field using a rate-independent model

instructive to compare the results to those that would be obtained with the corresponding rate-independent model presented in Sect. 4. In fact, to get a complete picture, we will consider not only dynamic delamination, but also alternative approaches that exploit static equilibrium equations, with inertial forces neglected. Formally, this can be done by setting the bar density ρ to zero. By exhausting all possible combinations of basic assumptions, we will be able to separately assess the effect of inertia and the effect of rate dependence incorporated in the damage law.

The assumptions regarding inertia (considered or neglected) and interface damage (rate-dependent or rate-independent) can be combined in four different ways. In Table 3, five lines are presented, because the case of no inertia combined with rate-independent damage can have two interpretations (but the results are essentially the same); see the last two lines referring to the "static" case.

Let us first discuss the **dynamic cases**, because they have already been analyzed. Line 1 summarizes the results obtained numerically for the rate-dependent model in Sects. 7.1–7.2, and line 2 presents the results that follow from the analytically derived formulae for the rate-independent model presented in Sect. 4.1. For the given set of material parameters from Table 1 and for relative crack speed $\alpha = 0.1$, formula (49) gives strain $\varepsilon_c = 3.587 \cdot 10^{-3}$, and the force per unit width $F_c/b = 0.845$ MN/m and end speed $v_c = 3.484$ m/s are then evaluated from slightly rearranged Eqs. (51)–(52).

Table 3 Comparison of response values obtained with various combinations of assumptions

Line	Case	$\dot{a}$ (m/s)	ρ (kg/m^3)	Damage model	τ_c (μs)	α	λ	$\tilde{\varepsilon}_c$	ε_c (10^{-3})	F_c/b (MN/m)	v_c (m/s)	G_c (J/m^2)
1	Dynamic	972	1600	Rate-dependent	5	0.1	0.995	0.7762	4.822	1.136	4.684	2711
2	Dynamic	972	1600	Rate-independent	0	0.1	∞	0.5774	3.587	0.845	3.484	1500
3	Quasi-static	972	0	Rate-dependent	5	0	1.	0.7748	4.789	1.128	4.653	2702
4	Static	972	0	Rate-independent	0	0	∞	0.5774	3.569	0.841	3.467	1500
5	Static	0				0	∞	0.5774	3.569	0.841	0	1500

Recall that the work of separation per unit delaminated area is, for the rate-independent model, automatically equal to the static fracture energy $G_{c0} = 1500$ J/m^2. By comparing these analytical results with the values in line 1 of Table 3 we find that rate effects increase the fracture energy by 81 %, while the applied force, end speed and strain in the delaminated part all increase by 34 %. This is not by chance, since F_c and v_c are proportional to ε_c, see Eqs. (42)–(43), and the dynamic fracture energy is proportional to ε_c^2, see (40). It is also worth noting that the rate-independent model is a limit case of the rate-dependent model, with characteristic time τ_c set to zero. The corresponding value of dimensionless parameter λ is infinity, because λ defined in (87) is inversely proportional to τ_c.

Now we proceed to the discussion of modeling approaches that neglect inertial forces. When this assumption is combined with a rate-dependent damage model, we refer to a **quasi-static case**; see line 3 in Table 3. Time still has its direct physical meaning, and faster processes need to overcome a higher resistance in terms of the force needed to drive the crack or fracture energy. However, since the density is set to zero, the "elastic wave speed" is infinite and it does not make sense to work with the relative crack speed (it would be zero for all finite values of absolute crack speed). To get a meaningful comparison, we consider the same value of absolute crack speed as in the dynamic cases, i.e., $\dot{a} = 972$ m/s. Even though $\alpha = 0$, parameter λ has a finite value, but it must be evaluated as $\lambda = l_0/(\dot{a}\tau_c)$. For the given parameters, we get $\lambda = 1$, which slightly differs from the value 0.995 obtained in the dynamic case for the same rate-dependent model. The corresponding $\tilde{\varepsilon}_c = 0.7748$ is computed numerically by solving the same problem as in the dynamic case, just with λ set to 1 instead of 0.995. When $\tilde{\varepsilon}_c$ is transformed into the actual strain, ε_c, it is now multiplied by u_f/l_0 while in the dynamic case it was multiplied by u_f/l with $l = l_0\sqrt{1-\alpha^2} = 0.995\, l_0$. The strain $\varepsilon_c = 4.789 \cdot 10^{-3}$ obtained in the quasi-static case turns out to be by 0.7 % lower than in the dynamic case, and the same relative decrease occurs for the force and end speed. The fracture energy is reduced only by 0.4 %. So the effect of inertia is, for the given crack speed, very small, much less important than the effect of rate dependence of damage evolution. Of course, this would no longer be true for higher crack speeds. If the quasi-static approach is used, there is no limit on the crack speed, while for the dynamic approach the force needed to drive the crack tends to infinity as the crack speed tends to the elastic wave speed.

When the inertial forces are neglected and the damage model is considered as rate-independent, time loses its physical meaning because the model does not possess any characteristic time. This case is referred to as **static**; see line 4 in Table 3. The response characteristics then do not depend on the crack speed. Parameter λ is infinite, and the value of $\tilde{\varepsilon}_c = \tilde{\varepsilon}_{c0} = 1/\sqrt{3}$ is the same as for the rate-independent damage model used in dynamics. However, the transformation to ε_c is now done using factor u_f/l_0 instead of u_f/l, and the result is by 0.5 % smaller than in the dynamic case. The same holds for the force and end speed, while the fracture energy is not reduced, since it is always equal to G_{c0} if the damage model is rate-independent.

In fact, most of the results presented in line 4 of Table 3 would remain the same for any other crack speed. This brings us to another interpretation of the static case, presented in line 5. Suppose that we consider the actual physical process as infinitely slow, i.e., we take the limit of $\dot{a} \to 0^+$. For such a process, it does not matter whether we set density to zero or to its real value, because the acceleration vanishes and so do the inertial forces. Also, it does not matter whether we consider the damage model as rate-dependent or rate-independent, because the damage

rate approaches zero and both types of formulation lead to the same response. The corresponding value of parameter $\alpha = \dot{a}/c = \dot{a}\sqrt{\rho/E}$ is zero because $\dot{a} = 0$ and $E > 0$ (so it does not matter whether we set $\rho = 0$ or $\rho > 0$), and parameter λ tends to infinity. This means that $\tilde{\varepsilon}_c = 1/\sqrt{3}$ can be expected to be obtained in the limit when $\lambda \to \infty$, independently of the value of A_c, which is the other dimensionless parameter that normally affects the outcome of the numerical procedure. The resulting force needed to drive the crack in a static way is F_{c0} given by formula (53), and the fracture energy is G_{c0}. These results are the same as for a non-zero crack speed handled by a model that neglects inertia forces and rate dependence of damage. The only difference between these cases (lines 4 and 5) is in the end speed, v_c. To make formula (52) applicable to the case when $\alpha = 0$ and $c = \infty$, it is good to divide both sides by α and rewrite the equation as

$$\frac{v_c^{(i)}}{\dot{a}} = \frac{\varepsilon_{c0}}{\sqrt{1-\alpha^2}} \tag{115}$$

For $\alpha = 0$, this gives $v_c^{(i)} = \varepsilon_{c0}\dot{a}$. So if the crack speed has a given nonzero value, as in line 4 of Table 3, we obtain a nonzero end speed $v_c^{(i)}$, in the present case equal to $3.569 \cdot 10^{-3} \times 972$ m/s $= 3.467$ m/s. In the limit of crack speed $\dot{a}$ approaching zero, $v_c^{(i)}$ tends to zero as well, but the ratio $v_c^{(i)}/\dot{a}$ tends to a known nonzero limit, $\varepsilon_{c0} = \sqrt{2G_{c0}/(hE)}$. Even though formula (52), and thus also (115), is valid for the rate-independent damage model only, the same limit of $v_c/\dot{a}$ would be obtained for the rate-dependent model. The reason is that when the relative crack speed α tends to zero, parameter λ tends to infinity and $\tilde{\varepsilon}_c$ tends to $\tilde{\varepsilon}_{c0}$ independently of the value of A_c.

7.4 Solution over the full range of crack speeds

Similar calculations as in Sect. 7.2 can be performed for other crack speeds. A special case arises for zero crack speed, because for $\dot{a} = 0$ equation (87) yields $\lambda = \infty$. Of course, it is not possible to use the numerical algorithm with parameter λ set literally to infinity, but one can use a very high value. The numerical results then become very close to the analytical solution for the rate-independent model, presented in Sect. 4.2.

Figure 6a shows the damage profiles in front of the crack tip and Fig. 6b shows the displacement profiles. The crack speed is seen to have a strong effect on these profiles, especially on the displacements. The solid curves that correspond to the zero crack rate in Fig. 6 have been constructed based on analytical expressions, and the dashed curves represent numerically computed results for crack speeds from $0.1\,c$ to $0.9\,c$. Fig. 6a also contains another solid curve constructed for the opposite extreme case, $\dot{a} = c$, which is just a theoretical limit.

The delamination zone (damage process zone) is bounded on one side by the crack tip, at which the damage variable is equal to 1, and on the other side it should be bounded by the point at which damage just starts growing. However, the present model uses a damage law with zero threshold, and so the damage variable is in theory greater than zero at all points of the interface. On the other hand, we know that damage decays to zero exponentially and from Figs. 5a and 6a it is clear that it becomes negligible at some finite distance from the crack tip. To be able to characterise the size of the delamination zone, we consider this zone as extending from the crack tip to the point where $D = 0.001$. Fig. 7a shows the dependence of the size of delamination zone on the relative crack speed. The solid curve corresponds to the rate-dependent model and, for comparison, the dashed curve shows the results for the rate-independent model, which can be analytically deduced from equations (56) and (59); see Sect. 9.3 for a deeper discussion.

It is interesting that, for the rate-independent model, the size of the delamination zone decreases with the crack speed while the opposite trend is obtained in the intermediate range of crack speeds in the rate-dependent case. Independently of the crack speed, the displacement obtained with the rate-independent model is a unique function of the dimensionless coordinate $\tilde{x} = \hat{x}/l$. With increasing crack speed $\dot{a}$, the characteristic length l decreases and tends to zero as $\dot{a}$ tends to the elastic wave speed, c. No matter which specific definition of the process zone size is used, this size scales with l and thus decreases with increasing crack speed. On the other hand, for the rate-dependent damage model, higher crack speeds in general lead to lower spatial gradients of damage and thus to longer delamination zones. Under steady dynamic conditions, the spatial gradient of damage is equal to the damage rate divided by the crack speed, and the damage rate cannot exceed the limit value $1/\tau_c$. This consideration also leads to the hypothetical limit distribution

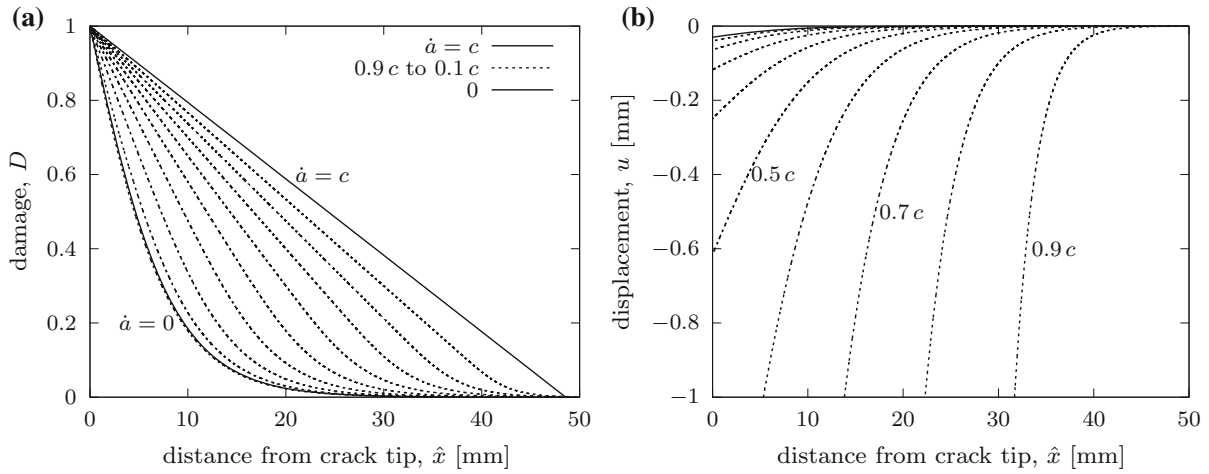

Fig. 6 Reference case, rate-dependent model, crack speeds $\dot{a}$ between $0.1\,c$ and $0.9\,c$ (dashed curves) and the extreme cases $\dot{a} = 0$ and $\dot{a} = c$ (solid curves): spatial distribution of **a** damage, **b** displacement

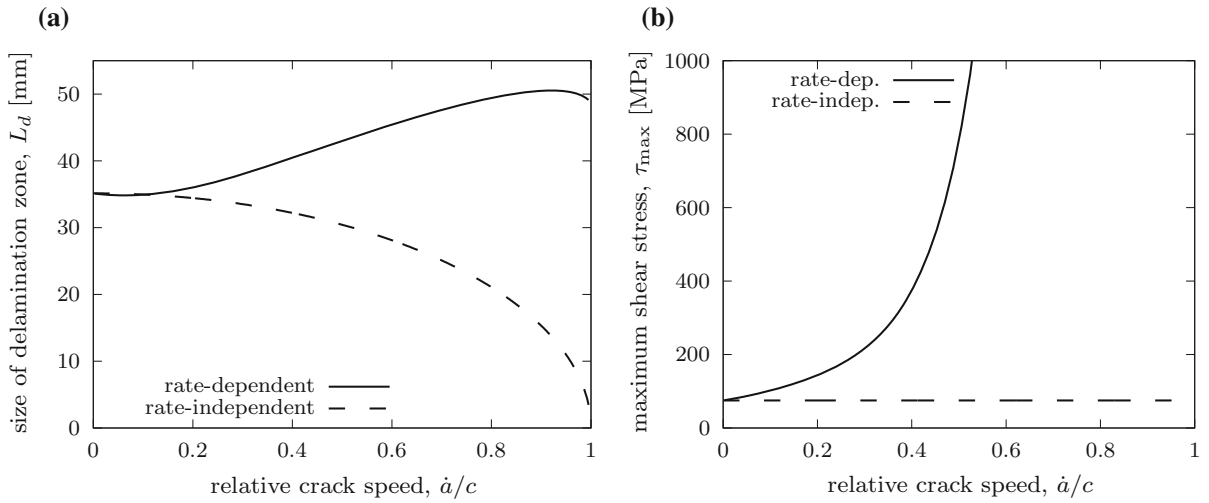

Fig. 7 Reference material: dependence of **a** size of delamination zone and **b** maximum shear stress on relative crack speed

of damage for crack speed equal to the elastic wave speed, plotted in Fig. 7a as the solid straight line with slope $1/(c\tau_c)$. For lower crack speeds, the damage rate is close to its limit value in a shorter zone near the crack tip and the damage profiles start at the crack tip with an almost linear segment that gets steeper as the crack speed decreases. For low crack speeds, the damage rates are also low and their bound controled by τ_c becomes irrelevant. The damage profiles then approach the analytical solution valid for the rate-independent model.

As seen in Fig. 7a, the size of the delamination zone obtained with the rate-dependent model remains between 34 and 51 mm, for all crack speeds. For comparison, the maximum shear stress that develops on the interface is plotted in Fig. 7b as function of the crack speed. The value of maximum shear stress starts at $\tau_{\max,0} = 75$ MPa for the static case and dramatically increases with increasing crack speed. For the rate-independent model, it would remain equal to 75 MPa for all crack speeds; see the dashed horizontal line.

In Fig. 8, the force needed to drive the crack at a constant speed is plotted against the crack speed. With increasing crack speed, the force increases dramatically, but it remains finite for all crack speeds smaller than c. This becomes clear from the graph in Fig. 8b,

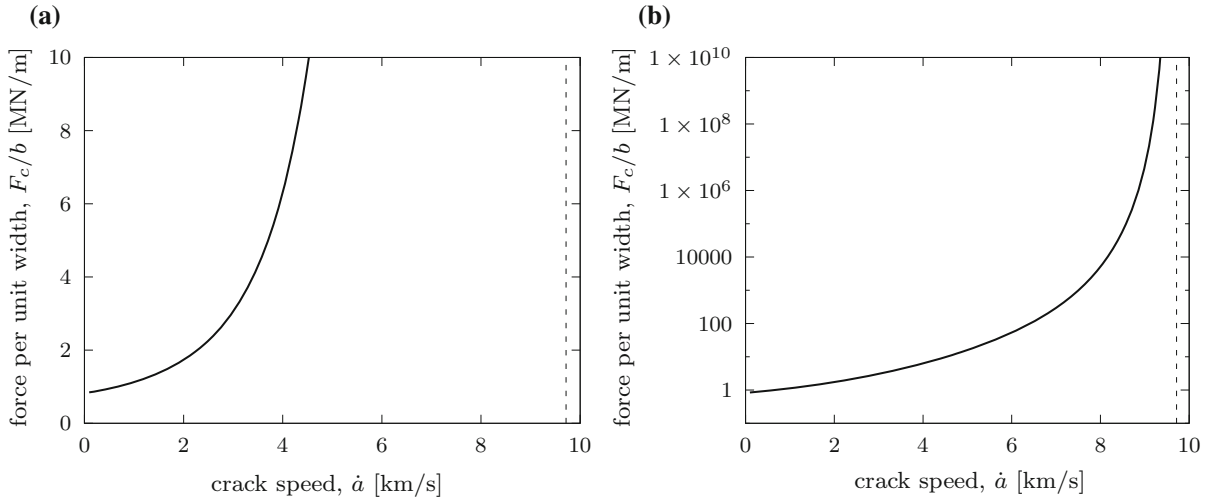

Fig. 8 Reference case, force (per unit width) needed to drive the crack at different speeds: **a** linear scale, **b** logarithmic scale on the vertical axis; the thin vertical line corresponds to the elastic wave speed

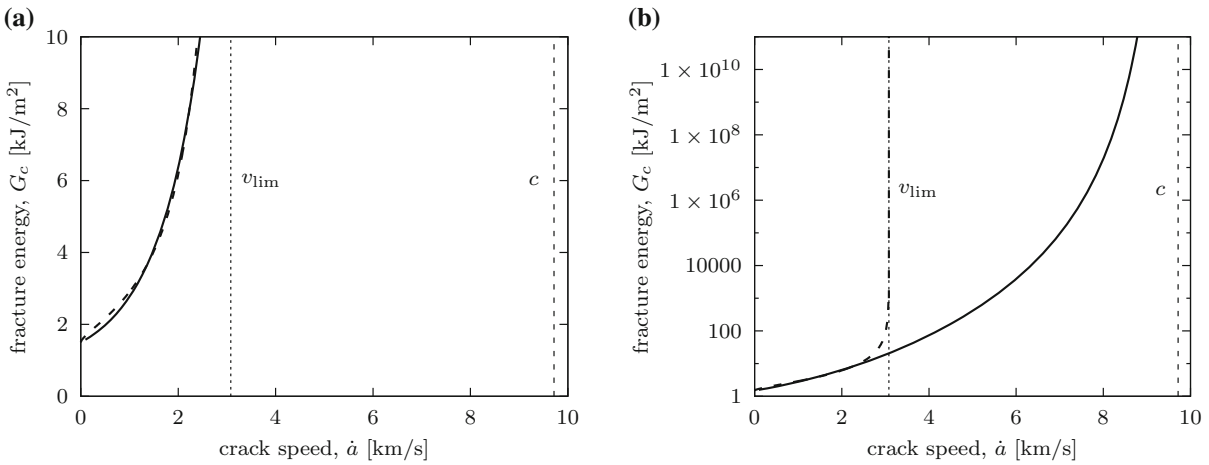

Fig. 9 Reference case, fracture energy for cracks at different speeds: **a** linear scale, **b** logarithmic scale on the vertical axis; the thin dashed vertical line corresponds to the elastic wave speed and the thin dotted vertical line corresponds to the "limit crack speed"

which is plotted in logarithmic scale on the vertical axis. The fracture energy, G_c, is represented by the thick solid curve in Fig. 9, again both in linear and semilogarithmic scales.

For instance, for a crack propagating at 82 % of the elastic wave speed, the force is 3000 times larger and the fracture energy is by 7 orders of magnitude larger than in the static case, so it becomes virtually impossible to drive the crack that fast. Also, even if such a high force could be exerted, the resulting normal stress would be extremely high and the material would hardly be able to transmit it. Therefore, our analysis of the behavior for crack speeds close to the elastic wave speed is related to the mathematical properties of the model rather than to the real physical response. The analysis reveals that a formulation with bounded damage rate does not lead to any reduction of the theoretical crack speed limit.

In Guimard et al. (2009), inspired by an idea proposed in Kanninen and Popelar (1985), a fitting of the rate-dependent fracture energy over the range of experimentally accessible crack speeds was proposed. For the given studied composite material, the maximum accessible crack speed was about 2000 m/s. In fact, for

higher speeds the computed strain would exceed the limit strain of the tested material. The proposed fitting was based on the empirical formula

$$G_c(\dot{a}) = \frac{G_{c0}}{1 - \left(\dfrac{\dot{a}}{v_{\text{lim}}}\right)^m} \tag{116}$$

where m is an exponent with typical values between 0.5 and 0.9, and v_{lim} is a parameter with the dimension of velocity. The optimal values of v_{lim} and m were then determined by fitting numerical data extracted from finite element analyses. If the fitting procedure is applied to the present numerical results in the range of crack speeds between 0 and 2400 m/s, the resulting optimal parameters are $v_{\text{lim}} = 3080$ m/s and $m = 0.646$. In the considered range, the agreement between accurately computed numerical results (solid curve) and approximation formula (116) (dashed curve) is quite good; see Fig. 9a. Nevertheless, the notation v_{lim} used in Guimard et al. (2009) and the denomination limit speed used in this paper were misleading. In fact, as it clearly appears from Fig. 9b, the theoretical limit speed for the proposed rate-dependent model is actually c.

8 Parametric analysis

Let us now systematically explore the role of individual parameters and the overall behavior of the system. After conversion to dimensionless form, the equations to be solved are (83) and (88). The solution depends on parameters λ and A_c. Parameter A_c is one of two parameters of the rate-dependent damage law (the other parameter being τ_c). Recall that parameter λ introduced in (87) is given by

$$\lambda = \lambda_0 \sqrt{\frac{1}{\alpha^2} - 1} \tag{117}$$

where

$$\lambda_0 = \frac{l_0}{c\tau_c} = \sqrt{\frac{Eh}{k}}\frac{1}{c\tau_c} = \frac{1}{\tau_c}\sqrt{\frac{h\rho}{k}} \tag{118}$$

is a dimensionless material parameter that depends on the mass of the bar per unit area of the interface, $h\rho$, elastic interface stiffness, k, and characteristic time of damage growth, τ_c. While λ_0 is a material parameter, the value of λ depends not only on the material but also on the relative crack speed, $\alpha = \dot{a}/c$.

The limit $\lambda \to \infty$ corresponds to the static case with $\dot{a} = 0$, and $\lambda = 0$ corresponds to the other extreme crack speed, $\dot{a} = c$. To get a more natural relation between the crack speed and the dimensionless parameter, let us define a new parameter $\mu = 1/\lambda^2$ and transform (117) into

$$\mu = \mu_0 \frac{\alpha^2}{1 - \alpha^2} = \mu_0 \frac{\dot{a}^2}{c^2 - \dot{a}^2} \tag{119}$$

where

$$\mu_0 = \frac{1}{\lambda_0^2} = \frac{k\tau_c^2}{h\rho} \tag{120}$$

By inversion, the relative crack speed can be expressed in terms of the ratio μ/μ_0 as

$$\alpha = \sqrt{\frac{\mu/\mu_0}{1 + \mu/\mu_0}} \tag{121}$$

For example, cases with $\mu = 0.1\,\mu_0$, μ_0 and $10\,\mu_0$ correspond to relative crack speeds $\alpha = \dot{a}/c \approx 0.30$, 0.71 and 0.95.

One advantage of using parameter μ instead of λ is that equation (88) can be rewritten as

$$-\sqrt{\mu}\,\tilde{D}'(\tilde{x}) = 1 - \mathrm{e}^{-A_c(\tilde{u}(\tilde{x}) - \tilde{g}^*(\tilde{D}(\tilde{x})))} \tag{122}$$

and the static limit is easily obtained by setting $\mu = 0$. In this special case, (122) reduces to $\tilde{u}(\tilde{x}) = \tilde{g}^*(\tilde{D}(\tilde{x}))$, which is the inverse dimensionless form of the rate-independent damage law $D = g(u)$. In general, the boundary value problem consisting of differential equations (122) and (83) combined with boundary conditions (89)–(91) is solved numerically. For each combination of parameters μ and A_c, the corresponding value of $\tilde{\varepsilon}_c = -\tilde{u}'(0)$ can be computed. Therefore, $\tilde{\varepsilon}_c$ can be considered as an implicitly defined function of μ and A_c. Once this function becomes available, it is straightforward to evaluate the dependence of various physical quantities of interest (force, bar end speed, fracture energy) on the crack speed. The key point is that this can be done for an arbitrary combination of material parameters such as E, ρ, h, k, G_{c0}, or τ_c. The influence of these physical properties is fully captured

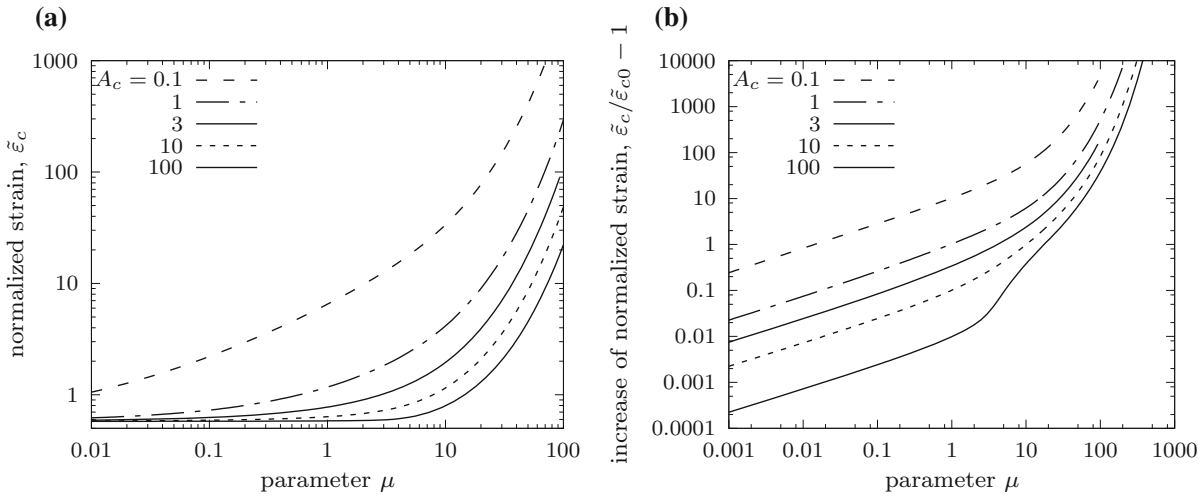

Fig. 10 Master curves showing the dependence of **a** normalised strain, $\tilde{\varepsilon}_c$, and **b** relative increase of normalised strain with respect to the static value, $\tilde{\varepsilon}_c/\tilde{\varepsilon}_{c0} - 1$, on dimensionless parameter $\mu \equiv 1/\lambda^2$ for various values of parameter A_c

by the transformation between μ and $\dot{a}$, and a complete description of the system reduces to a dimensionless function $\tilde{\varepsilon}_c$ of two dimensionless arguments, μ and A_c. Graphically, this function can be presented by plotting the dependence of $\tilde{\varepsilon}_c$ on μ for several selected values of A_c. Such graphs will be referred to as the master curves.

Master curves for a model built as a rate-dependent extension of the damage power law (6) with exponent $n = 1$ (i.e., with the dimensionless inverse damage function $\tilde{g}^*$ given by (86)) are plotted in Fig. 10a in logarithmic scale, which makes it possible to cover an extremely wide range. Parameter A_c has been set to 3 as a typical value (see the thick solid curve), and then to 0.1, 1, 10 and 100 for comparison, to show the influence on the master curve. In all cases, $\tilde{\varepsilon}_c$ monotonically increases with increasing μ. In the limit of $\mu \to 0^+$, all curves approach the same value, independent of A_c. This unique limit value represents the normalized strain that would be obtained with the rate-independent version of the model, for which A_c plays no role. In Sect. 4.1 it was shown that the strain at the crack tip, ε_{c0}, is for the rate-independent model given by (50), and the corresponding normalized strain is

$$\tilde{\varepsilon}_{c0} = \frac{l_0}{u_f}\varepsilon_{c0} = \sqrt{\frac{Eh}{k}}\frac{1}{u_f}\sqrt{\frac{2G_{c0}}{hE}} = \frac{1}{u_f}\sqrt{\frac{2G_{c0}}{k}} \tag{123}$$

For the presently considered power damage law with exponent $n = 1$, the area under the static cohesive curve is $G_{c0} = ku_f^2/6$, and so $\tilde{\varepsilon}_{c0} = 1/\sqrt{3}$. In general, $\tilde{\varepsilon}_{c0}$ is a dimensionless constant related to the shape of the cohesive diagram. Numerical results plotted in Fig. 10a indeed tend to $1/\sqrt{3}$ as μ tends to zero. To better show the initial trend at low crack speeds (i.e., for small values of μ), the graphs are replotted in Fig. 10b with $\tilde{\varepsilon}_c/\tilde{\varepsilon}_{c0} - 1$ on the vertical axis; more detailed discussion will follow in Sect. 9.3. Even though the shape of the curve for the very high value $A_c = 100$ may seem unusual, it is the correct one and has been verified using numerical calculations with high accuracy.

From a master curve with $\tilde{\varepsilon}_c$ plotted as function of $\mu \equiv 1/\lambda^2$, we can construct (for a given set of material parameters) the corresponding curves with various physical quantities plotted as functions of the crack speed. Primary physical quantities of interest include the force needed to drive the crack, F_c, the speed at which the free end of the bar is moving during steady crack propagation, v_c, and the fracture energy, G_c. Let us start from the rate-dependent fracture energy G_c given by (40). Substituting expression (113) for strain ε_c and making use of definition (56) of length l, we obtain

$$\begin{aligned} G_c &= \tfrac{1}{2}h\varepsilon_c^2(E - \rho\dot{a}^2) = \tfrac{1}{2}h\frac{u_f^2}{l^2}\tilde{\varepsilon}_c^2(E - \rho\dot{a}^2) \\ &= \tfrac{1}{2}ku_f^2\tilde{\varepsilon}_c^2 \end{aligned} \tag{124}$$

For zero crack speed, the relation between G_{c0} and $\tilde{\varepsilon}_{c0}$, already derived in (123), is recovered as a special case. Since $G_{c0} = ku_f^2\tilde{\varepsilon}_{c0}^2/2$, equation (124) can be rewritten as

$$G_c = G_{c0}\frac{\tilde{\varepsilon}_c^2}{\tilde{\varepsilon}_{c0}^2} \tag{125}$$

Let us emphasize that $\tilde{\varepsilon}_{c0}$ is a dimensionless constant dependent exclusively on the shape of the rate-independent cohesive curve. For the damage law considered here, we have $\tilde{\varepsilon}_{c0} = 1/\sqrt{3}$ and formula (125) reads $G_c = G_{c0}\tilde{\varepsilon}_c^2/3$.

The force needed to drive the crack at the given crack speed, F_c, and the speed of the fully delaminated zone, v_c, can be obtained from equations (45)–(46), rewritten here as

$$\begin{aligned} F_c &= b\sqrt{2hEG_c}\,\frac{1}{\sqrt{1-\alpha^2}} \\ &= b\sqrt{2hEG_{c0}}\,\frac{\tilde{\varepsilon}_c}{\tilde{\varepsilon}_{c0}}\,\frac{1}{\sqrt{1-\alpha^2}} \\ &= \frac{\tilde{\varepsilon}_c}{\tilde{\varepsilon}_{c0}}\,\frac{F_{c0}}{\sqrt{1-\alpha^2}} = \frac{\tilde{\varepsilon}_c}{\tilde{\varepsilon}_{c0}}\,F_c^{(i)} \end{aligned} \tag{126}$$

$$\begin{aligned} \frac{v_c}{c} &= \sqrt{\frac{2G_c}{hE}}\,\frac{\alpha}{\sqrt{1-\alpha^2}} = \sqrt{\frac{2G_{c0}}{hE}}\,\frac{\tilde{\varepsilon}_c}{\tilde{\varepsilon}_{c0}}\,\frac{\alpha}{\sqrt{1-\alpha^2}} \\ &= \frac{\tilde{\varepsilon}_c}{\tilde{\varepsilon}_{c0}}\,\frac{v_c^{(i)}}{c} \end{aligned} \tag{127}$$

Recall that $F_c^{(i)}$ and $v_c^{(i)}$ are the force and the bar end speed evaluated for the rate-independent model at the same crack speed, and F_{c0} is the static force (i.e., the force in the limit of crack speed approaching zero).

From the expressions in (125)–(127) combined with (120)–(121) it is clear that the master curves in Fig. 10a contain complete information on rate effects for all possible combinations of parameters. For a given material, the corresponding value of μ_0 can be evaluated from (120), and parameter μ can then be mapped onto the relative crack speed using formula (121). For instance, for the reference material parameters listed in Table 1, the value of μ_0 is about 100. This means that $\mu = 100$ corresponds to the relative crack speed $\dot{a}/c \approx 0.71$. In Fig. 10a we can see that for this value of μ and for $A_c = 3$, the value of $\tilde{\varepsilon}_c$ is about 100, and thus the fracture energy is about 30,000 times larger than in the static limit, as follows from equation (125) with $\tilde{\varepsilon}_{c0} = 1/\sqrt{3}$, and the force needed to drive the crack at this speed is about 250 times larger than in the static limit, as follows from equation (126) with $\tilde{\varepsilon}_{c0} = 1/\sqrt{3}$ and $\alpha = 0.71$. On the other hand, $\mu = 10$ corresponds to the relative crack speed $\dot{a}/c \approx 0.3$, and the value of $\tilde{\varepsilon}_c$ found in Fig. 10a for $A_c = 3$ is about 2 (a more precise value is 1.86). Thus the fracture energy would be roughly 12 times larger than in the static limit (more precisely, 10.4 times larger), and the force would be about 3.4 times larger. This is consistent with the previous results obtained for the particular material properties and presented in Figs. 8, 9. The advantage of the dimensionless master curves is that they are applicable to other combinations of material properties (and other bar thicknesses). For a bar with $\mu_0 = 10$, the increase of fracture energy by one order of magnitude would occur at relative crack speed around 0.7 (provided that A_c is still equal to 3).

Based on the master curves and on equations (120)–(121) and (125)–(127), it is easy, for each specific combination of material parameters and bar thickness, to transform the master curve into the corresponding plots of normalized force F/F_{c0}, normalized speed v_c/c and normalized fracture energy G_c/G_{c0} versus normalized crack speed $\dot{a}/c$. For the reference set of parameters, such plots are shown in Fig. 11a–c. In linear or semilogarithmic scales, the force graph would have the same shape as in Fig. 8 and the fracture energy graph would have the same shape as in Fig. 9, just with dimensionless variables on both axes. To provide additional insight, the graphs in Fig. 11a, c show the normalized force increase and the normalized increase of fracture energy due to rate effects in logarithmic scale. The dashed lines correspond to analytical approximations (132)–(134), to be derived later.

The graphs can be replotted for various combinations of parameters, which is useful for identification of material properties from real tests. As an example, Fig. 11d shows the dependence of relative force increase on relative crack speed for three different combinations of parameters A_c and μ_0. Suppose that all material properties characterizing the rate-independent response have been identified from static tests and that the mass density ρ is known. The remaining unknown parameters are A_c and τ_c, and parameter τ_c is uniquely linked to μ_0 by (120). If only one dynamic delamination test is available and the measured data indicate that the applied force increased by 70% of the static value leads to the crack speed equal to 10% of the elastic wave speed, then it is possible to find many combinations of A_c and μ_0 that would reproduce this behaviour; three of

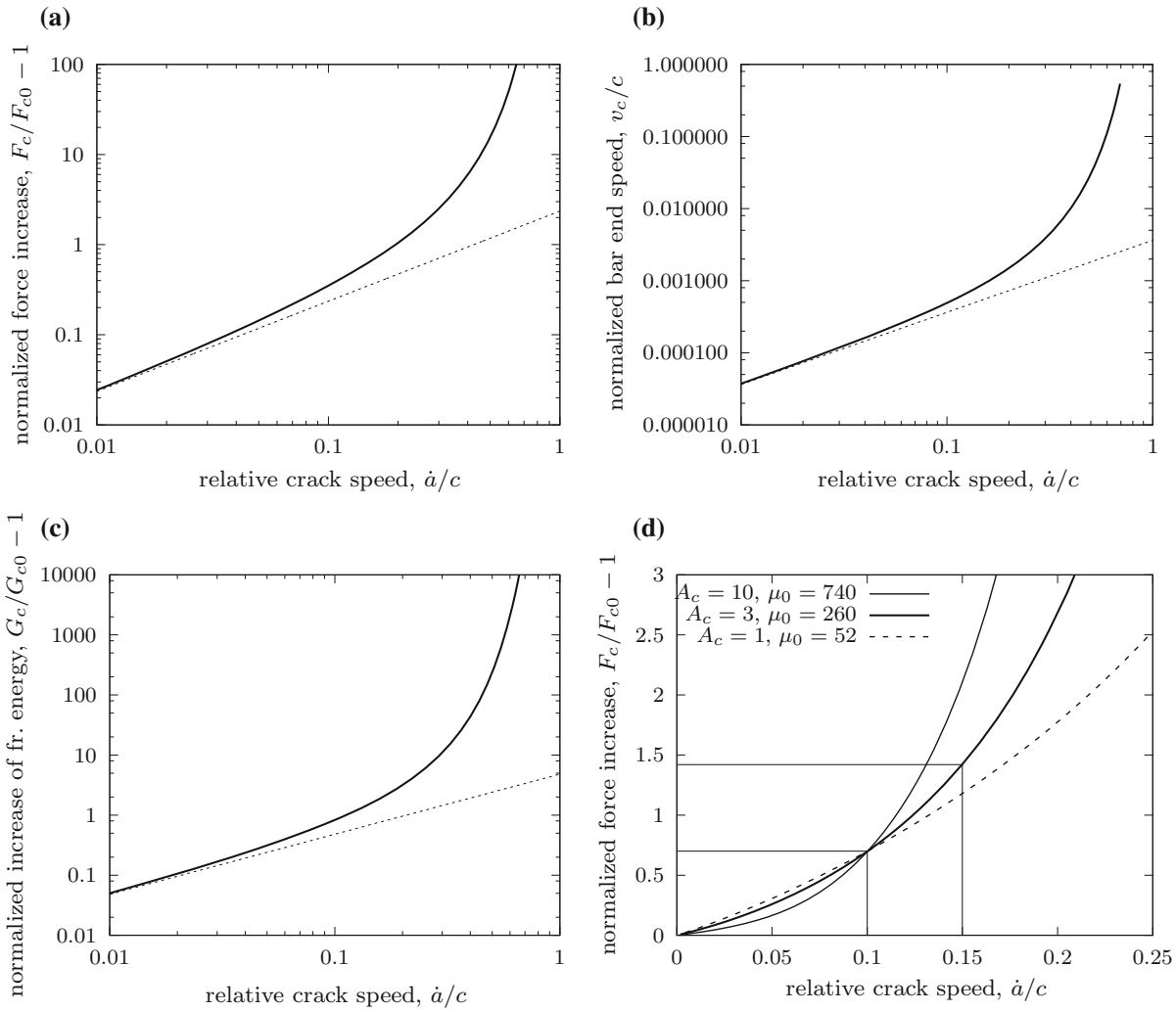

Fig. 11 Dependence of **a** relative force increase, **b** normalized bar end speed, and **c** relative increase of fracture energy on relative crack speed for the reference material with $A_c = 3$ and $\mu_0 = 100$; **d** dependence of relative force increase on relative crack speed for three sets of material parameters

them are shown in Fig. 11d. However, if an additional test shows that the applied force increased by 142% of the static value leads to the crack speed equal to 15% of the elastic wave speed, then the optimal combination of parameters $A_c = 3$ and $\mu_0 = 260$ can be uniquely identified from the graphs. Subsequently, parameter $\tau_c = \sqrt{h\rho\mu_0/k}$ can be determined from μ_0 and from the already available parameters (bar thickness, h, bar material density, ρ, and elastic interface stiffness, k).

9 Comparison between rate-dependent and rate-independent models

9.1 Global response characteristics

One objective of this paper is to analyse the differences caused by the extension to bounded-rate delayed damage as compared to the initial rate-independent version of the model. In fact, the best solution of this problem would be to derive an analytical expression reflecting

the combined effect of the two additional parameters introduced to describe the rate effect, τ_c and A_c. Unfortunately, such relations are not available, and one needs to rely on numerical determination of some characteristic curves, such as the relative increase of the critical strain, force or fracture energy. Nevertheless, some analytical insight may be obtained in the extreme cases of low or high crack speeds, which will be treated in Sects. 9.3–9.4.

Even though, for rate-independent models, the shape of the cohesive curve has no influence on the global rate effect, this is not necessarily the case for rate-dependent models. Therefore, the comparison will be made here not only for the power damage law (6) with exponent $n = 1$, which leads to a parabolic shape of the cohesive curve, but also for damage law (7), which leads to a triangular cohesive curve (i.e., to linear softening).

The inverse damage function for damage law (7) was specified in (79), and its dimensionless form is

$$\tilde{g}^*(D) = \frac{g^*(D)}{u_f} = \frac{u_p}{u_f - (u_f - u_p)D} = \frac{\eta}{1 - (1-\eta)D} \tag{128}$$

where $\eta = u_p/u_f$ is a dimensionless parameter that corresponds to the ratio between the displacement jump at peak stress, u_p, and displacement jump at full delamination, u_f. In this comparative calculation, all primary material parameters, including the interface stiffness k and the static fracture energy G_{c0}, are supposed to have the reference values specified in Table 1a. Formula $u_f = \sqrt{6G_{c0}/k}$, which was used for evaluation of the derived parameter u_f in Table 1b, is specific to the power damage law with exponent $n = 1$. In order to get the same value of u_f for the model with a triangular cohesive diagram, we need to set $u_p = u_f/3$, i.e., $\eta = 1/3$, because then $ku_pu_f/2 = ku_f^2/6$ and formula (10) gives the same result as formula (9) with $n = 1$. In the rate-independent case, the dependence of global characteristics (such as the fracture energy, strain in the fully delaminated segment, or applied force) on the crack speed would be the same for both cohesive laws, only the shapes of the damage and displacement profiles would differ. Let us note here that by enforcing k, u_f and G_{c0} to be the same for both cohesive diagrams, we obtain different values of the maximum shear stress, as shown in the bottom part of Fig. 2. The stress at the peak of the rate-independent cohesive diagram is given by $\tau_{max} = k\eta u_f = ku_f/3$ for the triangular diagram with $\eta = u_p/u_f = 1/3$, and by $\tau_{max} = ku_f/4$ for the parabolic diagram.

The graphs presented in Figs. 12–14 have been constructed for material parameters presented in Table 1, except for the value of characteristic time τ_c, whose effect is examined in Fig. 12. In order to assess the rate effects, it is instructive to compare, for a given applied force, the crack speeds obtained for the rate-independent model and for the rate-dependent model with various values of τ_c. Recall that the rate-independent model can be considered as a limit case of the rate-dependent one, with τ_c set to zero. For each fixed value of the applied force, increasing τ_c leads to a reduction of the crack speed; see Figs. 12a, c. In Guimard et al. (2009), the bounded-rate delayed damage formulation was introduced to reproduce the measured crack speed, which otherwise would have been between three and four times larger. It appears that, for the treated example characteristic of a delamination mode-II specimen, the results are very sensitive to the value of τ_c, especially for values close to 1 μs. Even for values around 2 μs, the rate effect is quite important, as noticed in Guimard et al. (2009). This is probably more obvious from Fig. 12b, d, where the relative increase of the applied force with respect to the rate-independent model is displayed as a function of the relative crack speed.

Even though the overall trend is the same, important differences exist between the results obtained with the rate-dependent extensions of two different damage functions. It turns out that rate effects are more pronounced for the model with a triangular cohesive diagram than for the parabolic one. The reason for these differences will be discussed in the next subsection.

9.2 Influence of shape of cohesive curve on the process zone and consequences for rate effects

Since all the primary parameters are kept the same, the differences between the global responses for the rate-dependent extensions of models with parabolic and triangular cohesive diagrams are due to the different forms of function $\tilde{g}^*$ presented in Fig. 13, which induce different profiles of damage and displacement jump along the process zone, depending of the relative crack speed. In Fig. 14a, c, the damage profiles for the two models are displayed for the reference parameters from Table 1. Due to the threshold of damage

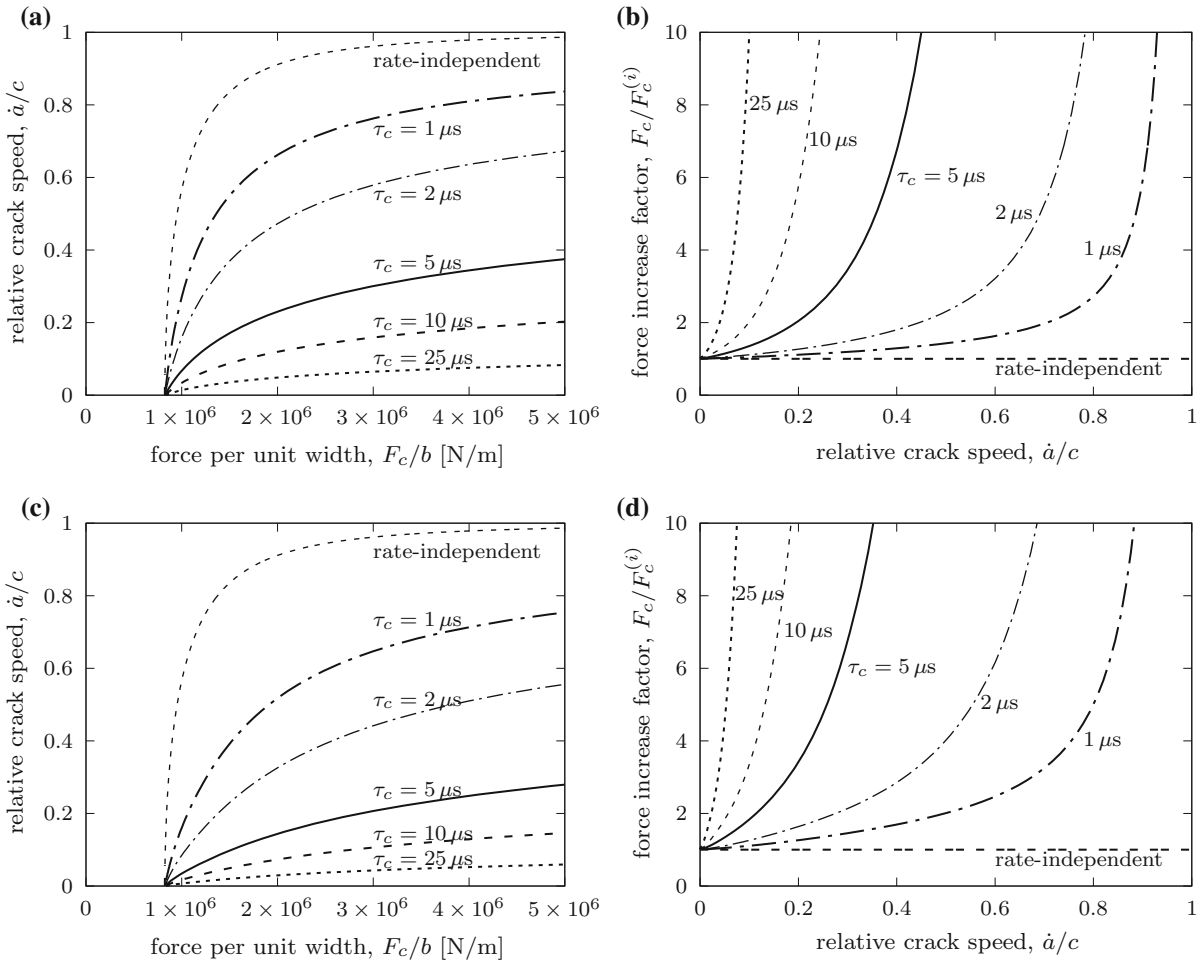

Fig. 12 Influence of the characteristic time τ_c on the crack speed as function of the applied load for **a** parabolic and **c** triangular cohesive curve; and the relative increase of the applied force with respect to the value obtained with the rate-independent model as function of the relative crack speed for **b** parabolic and **d** triangular cohesive curve; parameter $A_c = 3$ is fixed

introduced in the model with triangular cohesive diagram, the process zone is more concentrated than for the parabolic one. Therefore, the gradient of damage is more pronounced for the model with triangular diagram. Since the time derivative is related to the spatial derivative through the relation $\partial/\partial t = -\dot{a}\,\mathrm{d}/\mathrm{d}\hat{x}$, the damage rate is globally higher for the triangular model, which explains the more pronounced effect for that model. For relative crack speeds close to 1, the rate of damage approaches $1/\tau_c$ in a large part of the process zone for both models, which implies that those differences become less significant.

Another peculiar effect of the delayed damage formulation is that it extends the size of the process zone for increasing crack speed. For a rate-independent model, the damage profile depends on $\tilde{x} = \hat{x}/l$ only. Therefore in that case, as l decreases with the relative crack speed, the profile of the damage (i.e., the process zone) becomes more localised. The opposite trend is obtained for the rate-dependent model, at least for the parameters used in this example. It is to be noted that the size of the process zone is not a property of the interface only. In fact, it is a structural property, as is documented by the expression for the dimensionless parameter μ. Therefore, rate effects cannot be seen as intrinsic to the interface. For instance, it is impossible to express the fracture energy G_c as a unique function of the crack rate, $\dot{a}$, even if all properties of the interface (i.e., the static cohesive diagram and parameters A_c and τ_c) are fixed.

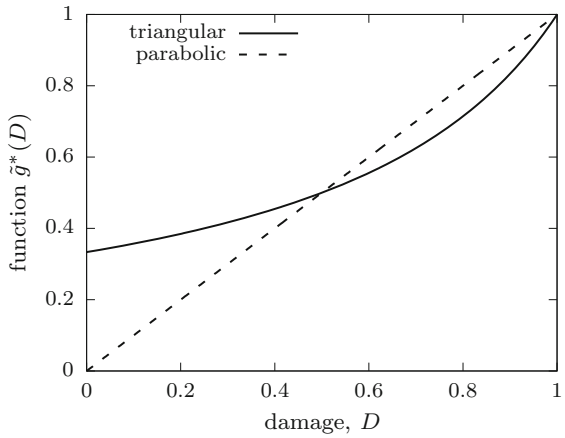

Fig. 13 Dimensionless inverse damage function $\tilde{g}^*$ for models with parabolic and triangular cohesive diagrams

9.3 Analytical approximation for low crack speeds

The case of low relative crack speed is of particular interest, since it is the one which is mostly encountered in experiments. To get a better idea about the initial increase of $\tilde{\varepsilon}_c$ (for small μ), the master curves were replotted in Fig. 10b in terms of the relative increase, defined as $\tilde{\varepsilon}_c/\tilde{\varepsilon}_{c0} - 1$, where $\tilde{\varepsilon}_{c0} = 1/\sqrt{3}$ is the value of $\tilde{\varepsilon}_c$ that corresponds to the zero-rate limit (for the model based on a parabolic cohesive diagram). From this graphical representation it is clear that, in a certain range, the curves can be approximated by straight lines. It can be checked that the slope of these lines, which are plotted in logarithmic scale, is 1/2. Therefore, the increase of $\tilde{\varepsilon}_c$ is initially proportional to the square root of parameter μ. This can be theoretically justified by the fact that, for low crack speeds, $\tilde{u}$ can be expected to remain close to $\tilde{D}$ (i.e., to the value of $\tilde{g}^*(\tilde{D})$) and the exponential function in (122) can be approximately replaced by a linear one. The equation then reduces to a linear differential equation,

$$\epsilon \tilde{D}'(\tilde{x}) = \tilde{u}(\tilde{x}) - \tilde{D}(\tilde{x}) \tag{129}$$

and the dimensionless solution becomes dependent only on one dimensionless parameter, $\epsilon = \sqrt{\mu}/A_c$, and not on μ and A_c separately.

For low crack speeds, the value of ϵ is small. By asymptotic expansion of the solution in terms of powers of ϵ, one could construct an approximation of the displacement and damage fields valid for low crack speeds and show that the dependence of $\tilde{\varepsilon}_c$ on ϵ must have the form $\tilde{\varepsilon}_c = \tilde{\varepsilon}_{c0} + \tilde{\varepsilon}_{c1}\epsilon + O(\epsilon^2)$ where $\tilde{\varepsilon}_{c0} = 1/\sqrt{3}$ is the value of $\tilde{\varepsilon}_c$ obtained for $\mu = 0$ (static limit, see Sect. 4.1), and $\tilde{\varepsilon}_{c1}$ is some dimensionless constant. Since $\epsilon = \sqrt{\mu}/A_c$, the asymptotic expansion leads to the approximation

$$\tilde{\varepsilon}_c \approx \frac{1}{\sqrt{3}} + \tilde{\varepsilon}_{c1}\frac{\sqrt{\mu}}{A_c} \tag{130}$$

Instead of trying to find $\tilde{\varepsilon}_{c1}$ analytically, we can evaluate it by fitting of the numerically computed results for low values of μ, which leads to $\tilde{\varepsilon}_{c1} = 1/\sqrt{6}$.

Approximation (130) is valid for small values of μ, i.e., for low crack speeds, for which $\dot{a}/c \approx \sqrt{\mu/\mu_0}$ where $\mu_0 = k\tau_c^2/(h\rho)$; see (120). It is thus possible to rewrite (130) in terms of the crack rate as

$$\tilde{\varepsilon}_c \approx \frac{1}{\sqrt{3}} + \frac{\tau_c}{A_c}\sqrt{\frac{k}{6h\rho}}\frac{\dot{a}}{c} \tag{131}$$

Substituting this into (125)–(127), we construct first-order approximations

$$\frac{G_c}{G_{c0}} = \frac{\tilde{\varepsilon}_c^2}{\tilde{\varepsilon}_{c0}^2} = 3\,\tilde{\varepsilon}_c^2 \approx 1 + \frac{\tau_c}{A_c}\sqrt{\frac{2k}{h\rho}}\frac{\dot{a}}{c} \tag{132}$$

$$\begin{aligned}\frac{F_c}{F_{c0}} &= \frac{\tilde{\varepsilon}_c}{\tilde{\varepsilon}_{c0}}\frac{1}{\sqrt{1-\alpha^2}} = \frac{\sqrt{3}\,\tilde{\varepsilon}_c}{\sqrt{1-\alpha^2}} \\ &\approx \sqrt{3}\left(\frac{1}{\sqrt{3}} + \frac{\tau_c}{A_c}\sqrt{\frac{k}{6h\rho}}\frac{\dot{a}}{c}\right)\left(1 + \frac{\dot{a}^2}{2c^2}\right) \\ &\approx 1 + \frac{\tau_c}{A_c}\sqrt{\frac{k}{2h\rho}}\frac{\dot{a}}{c}\end{aligned} \tag{133}$$

$$\begin{aligned}\frac{v_c}{\dot{a}} &= \frac{v_c}{\alpha c} = \sqrt{\frac{2G_{c0}}{hE}}\frac{\tilde{\varepsilon}_c}{\tilde{\varepsilon}_{c0}}\frac{1}{\sqrt{1-\alpha^2}} \\ &\approx \sqrt{\frac{2G_{c0}}{hE}} + \frac{\tau_c}{A_c}\sqrt{\frac{G_{c0}k}{h^2E\rho}}\frac{\dot{a}}{c}\end{aligned} \tag{134}$$

which allow to compare the global characteristics for low crack speeds to those for infinitely slow crack propagation. The same first-order approximations are also valid when comparing the global characteristics for the rate-dependent model to the rate-independent one because the differences between the rate-independent quantities and the static limit case are of the second order in $\dot{a}/c$. Recall that, for the rate-independent damage model, the effect of inertia forces is reflected by the factor $1/\sqrt{1-\alpha^2}$, which is then in (133) approximated

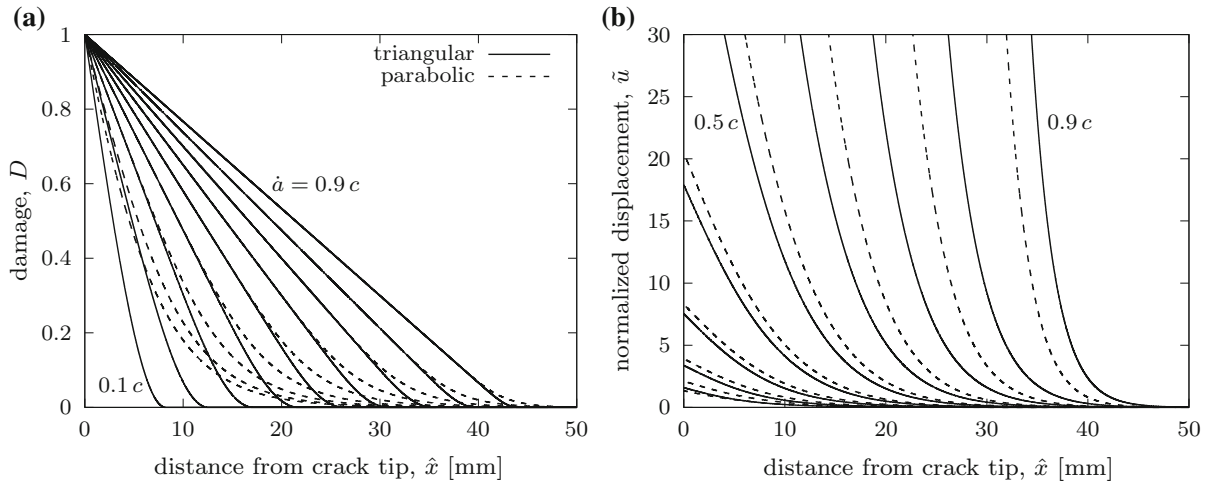

Fig. 14 Spatial distribution of **a** damage and **b** normalized displacement for rate-dependent extensions of models with parabolic and triangular cohesive diagrams, for crack speeds $\dot{a}$ between $0.1\,c$ and $0.9c$

by $1 + \dot{a}^2/(2c^2)$ and has no effect on the first-order expansion. The same holds for (134), where the intermediate step is skipped.

Since $c = \sqrt{E/\rho}$, approximation (132) could be rewritten in terms of the absolute crack speed as

$$\frac{G_c}{G_{c0}} \approx 1 + \frac{\tau_c}{A_c}\sqrt{\frac{2k}{hE}}\,\dot{a} \tag{135}$$

This shows that rate effect on the fracture energy does not solely depend on the interface characteristics but also on the stiffness of the elastic bar. The same could be said about the rate effect on the force and bar end speed; see (133)–(134).

From approximations (131)–(135) it can be deduced that the key parameter which controls the rate effect in the low-speed regime is the ratio τ_c/A_c. This is natural, since for slow processes the driving force $[\![u]\!] - g^*(D)$ remains small and if the exponential function in the damage evolution law (77) is expanded into Taylor series, the linear part of the approximation can be written as

$$D_{,t} = \frac{A_c^*}{\tau_c}\left([\![u]\!] - g^*(D)\right) = \frac{A_c}{\tau_c}\frac{[\![u]\!] - g^*(D)}{u_f}$$
$$= \frac{A_c}{\tau_c}\left(\tilde{u} - \tilde{g}^*(D)\right) \tag{136}$$

To be able to identify parameters A_c and τ_c separately, one should consider not only the regime of low crack speed but also the intermediate one. The opposite extreme case when τ_c alone is the main control parameter of the rate effect will be examined in Sect. 9.4.

The validity of approximations (132)–(133) is confirmed by the graphs in Fig. 15, which show the relative increase of the applied force and fracture energy with the relative crack speed, evaluated for the reference set of parameters, leading to $\mu_0 = 100$. The thick dashed curves correspond to the model with a parabolic cohesive diagram, for which the low-speed approximations are given by (132)–(133). Similar approximations can be constructed for the model with a triangular cohesive diagram, only the values of $\tilde{\varepsilon}_{c0}$ and $\tilde{\varepsilon}_{c1}$ need to be recalculated. The value of $\tilde{\varepsilon}_{c0}$ can be obtained analytically from equation (123), which has a general validity. For the triangular cohesive diagram, the static fracture energy is $G_{c0} = k u_p u_f/2$, and substituting this into (123) we get $\tilde{\varepsilon}_{c0} = \sqrt{u_p/u_f} = \sqrt{\eta}$. The particular choice in our examples is $\eta = 1/3$, and so $\tilde{\varepsilon}_{c0}$ has the same value $1/\sqrt{3}$ as for the model with the parabolic cohesive diagram, and equation (130) remains valid. The value of $\tilde{\varepsilon}_{c1}$ must be estimated numerically. For $\eta = 1/3$, the result is $\tilde{\varepsilon}_{c1} \approx 0.765$. Therefore, for the model with the triangular cohesive diagram, the factor $1/\sqrt{6}$ in equation (131) would need to be replaced by 0.765, and equations (132)–(134) would need to be modified accordingly. As a result, the dotted straight lines in both parts of Fig. 15 that represent the first-order approximation for the model with triangular diagram are vertically shifted with respect to the lines for the model with parabolic diagram. This means that if

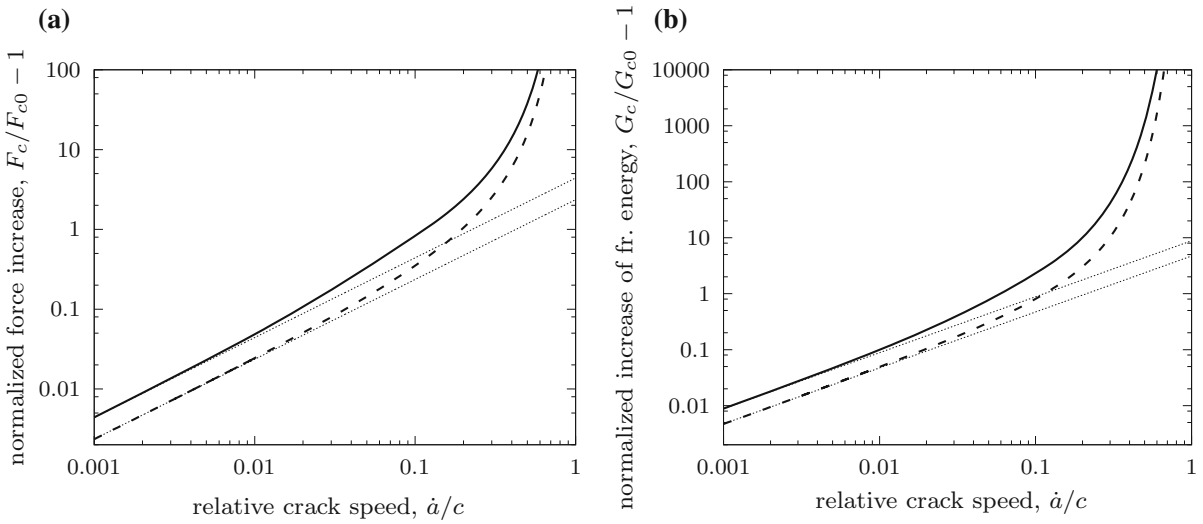

Fig. 15 Rate effects for the reference material from Table 1a with damage laws corresponding to parabolic (dashed) and triangular (solid) cohesive diagrams, and their linear approximation for low crack speeds (dotted)

all basic parameters remains the same, the model with triangular diagram gives a stronger rate effect. However, one could obtain the same rate effect (at least in the range of low crack speeds) for both models if the fraction τ_c/A_c is properly adjusted. For the model with triangular diagram, this fraction would need to be reduced by the factor $1/(0.765\sqrt{6}) \approx 0.534$ as compared to the model with parabolic diagram. This could be achieved by decreasing τ_c, by increasing A_c, or by combining both modifications.

An estimate of the size of damage process zone can be constructed by exploiting the analytical solution available for the rate-independent model (which also approximately applies to the rate-dependent model if the crack speed is very low). For the model with parabolic cohesive diagram, we can exploit the solution given by (59) with $n = 1$. Substituting $\hat{u} = -10^{-3}u_f$ (which corresponds to $D \approx 0.001$, considered as the conventional value defining the boundary of the process zone) and $l = l_0$, we obtain an analytical formula for the size of the process zone,

$$L_{d0} = 2l_0\left(\operatorname{atanh}\sqrt{1-\frac{2}{3}\times 10^{-3}} - \operatorname{atanh}\sqrt{\frac{1}{3}}\right) \tag{137}$$

For $l_0 = 4.76$ mm we get $L_{d0} = 35.14$ mm, which is an agreement with the values plotted in Fig. 7a in the range of $\dot{a}/c \le 0.2$.

For the model with triangular cohesive diagram, the boundary of the process zone is well defined because damage remains equal to zero for $[\![u]\!] \le u_p$. In the rate-independent case, the size of the process zone is equal to $\hat{x}_e$ given by formula (71) that was derived in Sect. 4.2.2. At low crack speeds, this can also be used as an estimate for the rate-dependent model. Substituting $l = l_0$ and $u_p = \eta u_f$ into (71), we obtain

$$L_{d0} = l_0\sqrt{\frac{1-\eta}{\eta}}\arctan\sqrt{\frac{1-\eta}{\eta}} \tag{138}$$

For $l_0 = 4.76$ mm and $\eta = 1/3$, this gives $L_{d0} = 10.54$ mm, which is in agreement with the damage profiles for $\dot{a}$ up to $0.2\,c$ plotted by solid curves in Fig. 14a.

9.4 Analysis for high crack speeds

Figure 14a indicates that, for crack speeds approaching the elastic wave speed, the shape of the damage profile is almost linear, at least in some range. This is not by chance. For high crack speeds, damage must propagate fast, but the maximum damage rate dictated by the delayed damage law (77) is $1/\tau_c$. The maximum damage rate is approached when the difference $[\![u]\!] - g^*(D)$ becomes much larger than $1/A_c^* = u_f/A_c$. Since $g^*(D) \le u_f$, the condition is certainly satisfied if the displacement jump becomes much larger

than $u_f(1 + 1/A_c)$. In that case, the right-hand side of equation (122) can be approximately replaced by 1, and the corresponding damage distribution is then described by:

$$\tilde{D}(\tilde{x}) \approx 1 - \frac{\tilde{x}}{\sqrt{\mu}} \tag{139}$$

Of course, this formula is applicable only for $\tilde{x} \in [0, \sqrt{\mu}]$ and becomes somewhat inaccurate near the right end of this interval. In dimensionless form, the size of the delamination zone can be estimated as $\sqrt{\mu}$. To get the real physical size, we must transform $\tilde{x}$ to $\hat{x} = l\tilde{x}$, which means that the size of the delamination zone at high crack speed is expressed as:

$$L_{d1} \approx l\,\sqrt{\mu} = \dot{a}\tau_c \tag{140}$$

Since this estimate is valid for crack speeds close to the elastic wave speed, we can replace $\dot{a}$ by c. For the reference set of parameters, this leads to

$$L_{d1} \approx c\,\tau_c = 9715 \times 5 \times 10^{-6}\,\mathrm{m} = 48.575\,\mathrm{mm} \tag{141}$$

which agrees well with the damage profiles plotted in Fig. 14a for $\dot{a}/c$ close to 1; see also Fig. 7a. Note that this estimate does not depend on the shape of cohesive diagram (parabolic, triangular, or any other), since the high-speed limit of the damage profile is controled exclusively by parameter τ_c and by the elastic wave speed.

10 Conclusions

The proposed simplified model for mode-II interfacial crack propagation combined with a direct shooting method adapted to the case of self-similar crack propagation has allowed to characterize rate effects induced by incorporation of rate dependence into the damage law. The rate effects have been studied by looking at the relations between the crack speed and global characteristics such as fracture energy, applied force, and the speed of the end section on which the force is acting. The main results can be summarized as follows:

- For a rate-independent formulation, the solution can be derived analytically, at least for the types of damage function considered here. The fracture energy is in this case independent of the crack speed and equal to its static value. The relation between other global characteristics (such as the applied force and the end speed) and the crack speed can be described in closed form, and the effects of inertia are characterized by universal functions, independent of the specific form of the damage law.
- For a rate-dependent formulation based on a bounded-rate damage law, the problem can be converted into a dimensionless form and the solution then depends exclusively on two dimensionless variables, provided that the type of the underlying damage law is fixed. Graphically, the response of the system in dimensionless format can be characterized by a family of so-called master curves. By transforming back into the physical space, the global characteristics can be deduced and the role of all physical parameters can be elucidated.
- For slow crack propagation, the increase of the applied force or end speed is approximately proportional to the crack speed.
- In general, the fracture energy, applied force and end speed increase with increasing crack speed but remain finite for all crack speeds lower than the elastic wave speed. Therefore, the bounded-rate damage formulation does not lead to any reduction of the maximum possible crack speed.
- From the practical point of view, the increase of the applied force and consumed energy as functions of crack speed is so dramatic that the crack speed that can actually be attained in real tests becomes limited.
- Even in a self-similar process, the rate effects are governed by the process zone. The spatial distribution of displacement jump along this zone determines the variation of the displacement jump rate in time at a fixed point and thus also the fracture energy. For a given geometrical setup (in the present paper a thin semi-infinite layer bonded to a rigid substrate), one can describe the fracture energy as function of the crack speed. However, if the geometry is changed, the characteristics of the process zone would change as well and the dependence of fracture energy on crack speed would be modified. In this sense, rate effects cannot be seen as intrinsic to the interface.

Approaches used in this paper could be applied without problems to other rate-dependent damage models

and it would be interesting to compare in the same manner the properties of those models. It would be interesting to extend the analysis to mode-I and mixed-mode interfacial crack propagations.

Acknowledgements This research has been financially supported by the European Regional Development Fund through the Center of Advanced Applied Sciences at the Czech Technical University in Prague (Project No. CZ.02.1.01/0.0/0.0/16_019/0000778).

Appendix: Peeling test

Mode-II delamination can be regarded as a special case of the peeling test, in which an elastic strip is detached from a rigid substrate by a force F_c that pulls in an inclined direction, under a prescribed angle θ; see Fig. 16a. If the peeling process is considered as rate-independent, the energy balance equation written for a steady process contains terms that represent the external work, energy dissipated by debonding, increase of potential energy of elastic deformation and increase of kinetic energy. For an increment in which the length of the debonded zone increases by da, the energy balance equation can be written as

$$F_c\,\mathrm{d}u = G_{c0}b\,\mathrm{d}a + \tfrac{1}{2}E\varepsilon_c^2 bh\,\mathrm{d}a + \tfrac{1}{2}\rho v^2 bh\,\mathrm{d}a \quad (142)$$

where du is the distance by which the loaded end of the sheet subjected to force F_c moves in the direction aligned with the force, ε_c is the axial strain in the debonded sheet, and v is the constant speed at which this part moves. The left-hand side of (142) is the incremental supplied work, and the terms on the right-hand side correspond to the energy dissipated by creating a newly debonded area $b\,\mathrm{d}a$, elastic energy stored by stretching the newly debonded segment of volume $bh\,\mathrm{d}a$ to strain ε_c, and kinetic energy of the newly debonded segment that was initially at rest and after debonding is moving at speed v. It is worth noting that the first term on the right-hand side of (142), which represents the dissipated energy (or work of separation), is considered here as independent of angle θ. This means that mode mixity is assumed to have no influence on the energy needed to separate the surfaces. In the case of adhesion, this assumption is acceptable, as proven, e.g., by the experiments of Kendall (1975) performed on rubber crosslinked against a glass plate.

As shown in Fig. 16b, the distance du can be expressed as the difference between the length of the newly debonded stretched segment, d$a(1+\varepsilon_c)$, and the projection of the initial length of this segment, d$a\cos\theta$. Substituting

$$\mathrm{d}u = (1+\varepsilon_c)\mathrm{d}a - \cos\theta\,\mathrm{d}a \quad (143)$$

into (142) and dividing both sides by $b\,\mathrm{d}a$, we obtain

$$\frac{F_c}{b}(1+\varepsilon_c-\cos\theta) = G_{c0}+\tfrac{1}{2}Eh\varepsilon_c^2+\tfrac{1}{2}\rho h v^2 \quad (144)$$

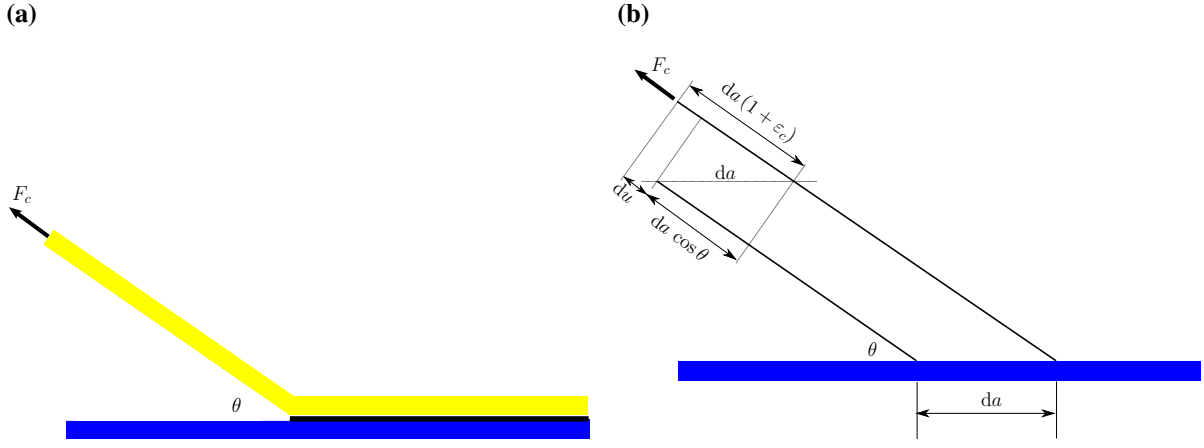

Fig. 16 **a** Schematic representation of the peeling test: elastic sheet (yellow) attached to a rigid substrate (blue) by an adhesive interface (black), pulled by a force F_c in a direction inclined by angle θ, **b** graphical evaluation of incremental displacement $\mathrm{d}u = \mathrm{d}a(1+\varepsilon_c) - \mathrm{d}a\cos\theta$ that corresponds to an increment of debonded length da

Since the sheet is assumed to be linear elastic, the strain is easily expressed as

$$\varepsilon_c = \frac{F_c}{Ebh} \tag{145}$$

From Fig. 16b it is also possible to deduce the speed at which the sheet end (and thus the entire debonded segment) moves. The horizontal component of the displacement of the sheet end is $\mathrm{d}a - \mathrm{d}a(1+\varepsilon_c)\cos\theta$ and the vertical component is $\mathrm{d}a(1+\varepsilon_c)\sin\theta$. Consequently, the speed of the delaminated part, v, can be linked to the crack speed, $\dot{a}$, by the relation

$$\begin{aligned} v &= \dot{a}\sqrt{(1-(1+\varepsilon_c)\cos\theta)^2 + ((1+\varepsilon_c)\sin\theta)^2} \\ &= \dot{a}\sqrt{(1+\varepsilon_c)^2 - 2(1+\varepsilon_c)\cos\theta + 1} \end{aligned} \tag{146}$$

Substituting (145) and (146) into (144), we construct a quadratic equation for the force F_c. The derivation is somewhat easier to manage if we consider ε_c instead of F_c as the primary unknown. Equation (144) with F_c replaced by $Ebh\varepsilon_c$ and with v expressed according to (146) reads

$$\begin{aligned} Eh\varepsilon_c(1+\varepsilon_c-\cos\theta) &= G_{c0} + \tfrac{1}{2}Eh\varepsilon_c^2 \\ &+ \tfrac{1}{2}\rho h\dot{a}^2\left((1+\varepsilon_c)^2 - 2(1+\varepsilon_c)\cos\theta + 1\right) \end{aligned} \tag{147}$$

When (147) is divided by Eh and the fraction ρ/E is replaced by $1/c^2$ where c is the elastic wave speed, we obtain

$$\begin{aligned} \varepsilon_c(1+\varepsilon_c-\cos\theta) &= \frac{G_{c0}}{Eh} + \tfrac{1}{2}\varepsilon_c^2 \\ &+ \tfrac{1}{2}\frac{\dot{a}^2}{c^2}\left((1+\varepsilon_c)^2 - 2(1+\varepsilon_c)\cos\theta + 1\right) \end{aligned} \tag{148}$$

This is the energy balance equation in a dimensionless form, which can further be rewritten as

$$\begin{aligned} 2\varepsilon_c(1+\varepsilon_c-\cos\theta) &= 2\gamma + \varepsilon_c^2 \\ &+ \alpha^2\left((1+\varepsilon_c)^2 - 2(1+\varepsilon_c)\cos\theta + 1\right) \end{aligned} \tag{149}$$

where $\alpha = \dot{a}/c$ is the relative crack speed and

$$\gamma = \frac{G_{c0}}{Eh} \tag{150}$$

is a dimensionless parameter characterizing the ratio between the fracture energy and the elastic sectional stiffness per unit width. For stiff and weakly bonded sheets, this parameter is small compared to 1.

Equation (149) can be recast into a quadratic equation

$$\begin{aligned} &(1-\alpha^2)\varepsilon_c^2 + 2(1-\alpha^2)(1-\cos\theta)\varepsilon_c \\ &\quad - 2(\gamma + \alpha^2(1-\cos\theta)) = 0 \end{aligned} \tag{151}$$

with ε_c as the unknown variable. Since the coefficients at ε_c^2 and at ε_c are positive while the absolute term is negative, the equation has two real roots, one positive and one negative. Since the peeling test leads to tension, only the positive solution is physically meaningful, and so we get

$$\begin{aligned} \varepsilon_c &= \frac{-2(1-\alpha^2)(1-\cos\theta) + \sqrt{4(1-\alpha^2)^2(1-\cos\theta)^2 + 4(1-\alpha^2)2(\gamma+\alpha^2(1-\cos\theta))}}{2(1-\alpha^2)} \\ &= \sqrt{(1-\cos\theta)^2 + \frac{2\gamma + 2\alpha^2(1-\cos\theta)}{1-\alpha^2}} - (1-\cos\theta) \end{aligned} \tag{152}$$

This is the fully general solution, from which a number of special cases can be derived by various simplifications.

1. Static peeling test:
   Setting $\alpha = 0$, we obtain

$$\begin{aligned} \varepsilon_c &= \sqrt{(1-\cos\theta)^2 + 2\gamma} - (1-\cos\theta) \\ &= \sqrt{(1-\cos\theta)^2 + \frac{2G_{c0}}{Eh}} - (1-\cos\theta) \end{aligned} \tag{153}$$

$$\begin{aligned} F_c = Ebh\varepsilon_c &= b\sqrt{E^2h^2(1-\cos\theta)^2 + 2EhG_{c0}} \\ &- Ebh(1-\cos\theta) \end{aligned} \tag{154}$$

   This is the static solution, valid for slow tests in which the kinetic energy remains very small, and so the last term on the right-hand side of (144) can be neglected. A quadratic equation for F_c that corresponds to such a reduced version of (144) was constructed by Kendall (1975), who then validated formula (154) experimentally by performing peeling experiments at various angles on sheets of ethylene propylene rubber crosslinked against a glass

plate. In these tests, the rubber sheet thickness was $h = 0.75$ mm and the elastic modulus measured in tensile tests was $E = 1.21$ MPa. Kendall was aware of the fact that the debonding energy is actually rate-dependent and he adjusted the loading such that the crack speed was the same for all peeling angles (about 80 μm/s). At this speed, the debonding energy taken from Gent and Kinloch (1971) was $G_{c0} = 5$ J/m^2. The corresponding value of parameter $\gamma = G_{c0}/(Eh) = 5.5 \cdot 10^{-3}$ is much smaller than 1.

2. Static peeling test, stiff sheet:
Setting $\alpha = 0$ and $\gamma \ll 1$, we obtain

$$\varepsilon_c = (1-\cos\theta)\left(\sqrt{1+\frac{2\gamma}{(1-\cos\theta)^2}}-1\right) \approx (1-\cos\theta)\frac{\gamma}{(1-\cos\theta)^2} = \frac{\gamma}{1-\cos\theta} = \frac{G_{c0}}{Eh(1-\cos\theta)} \tag{155}$$

$$F_c = Ebh\varepsilon_c \approx \frac{bG_{c0}}{1-\cos\theta} \tag{156}$$

This case corresponds to a slow peeling test performed with a sheet which has a high axial stiffness (note that the assumption $\gamma \ll 1$ means that $Eh \gg G_{c0}$). In this case, the elastically stored energy is negligible compared to the dissipated energy, and the effect of axial strain on the external work (reflected in (144) by the term $F_c\varepsilon_c/b$) can be ignored, too. With these simplifications and under static conditions, the energy balance equation reduces to

$$\frac{F_c}{b}(1-\cos\theta) = G_{c0} \tag{157}$$

and formula (156) can be deduced directly, with no need to solve a quadratic equation. In fact, the same result could also be obtained by neglecting the quadratic term in equation (151). For $\alpha = 0$, the reduced linear equation for ε_c reads

$$2(1-\cos\theta)\varepsilon_c - 2\gamma = 0 \tag{158}$$

and its solution

$$\varepsilon_c = \frac{\gamma}{1-\cos\theta} \tag{159}$$

corresponds to (155).

3. Static mode-II delamination:
Setting $\alpha = 0$ and $\cos\theta = 1$, we obtain

$$\varepsilon_c = \sqrt{2\gamma} = \sqrt{\frac{2G_{c0}}{Eh}} \tag{160}$$

$$F_c = Ebh\varepsilon_c = b\sqrt{2EhG_{c0}} \tag{161}$$

In this case, the sheet is pulled in the direction parallel to the interface, which corresponds to the Mode-II delamination problem analyzed in the present paper. Naturally, the derived formula (161) corresponds to formula (53) from Sect. 4.1 (in which F_c is denoted as F_{c0}). Note that in this case it would not be correct to simplify equation (144) by setting $\varepsilon_c = 0$, even if the strain is actually small. The reason is that if angle θ vanishes, we have $\cos\theta = 1$ and ε_c is no longer negligible with respect to $1-\cos\theta$. Also, the term with ε_c^2 on the right-hand side of (144), which is related to the elastic energy, must not be deleted because it is of the same order as the left-hand side, which is related to external work. Since the left-hand side of (144) is proportional to the product of the force and strain, no external work would be supplied if the sheet were considered as infinitely stiff. This is a particular feature that distinguishes the special case of mode-II delamination ($\theta = 0$) from the peeling test in an inclined direction ($\theta > 0$). The elastic energy might be negligible for sufficiently large angles and stiff materials, but as the peeling angle tends to zero, this energy becomes important and in the limit case it is absolutely essential, as noticed already by Kendall (1975). The present formula (161) corresponds (in a somewhat different notation) to Kendall's formula (6), and the present formula (156) corresponds to Kendall's formula (5). In fact, the approximation used in (155) if γ is small with respect to $(1-\cos\theta)^2$, so for small peeling angles it is not sufficient to check that $\gamma \ll 1$. Indeed, the peeling forces reported in Kendall (1975) are very well approximated by (156) for peeling angles for which $1-\cos\theta$ is 0.2 or greater (i.e., $(1-\cos\theta)^2$ is at least 0.04 and exceeds $\gamma = 5.5\cdot 10^{-3}$ by an order of magnitude, but a clearly marked deviation is observed if $1-\cos\theta$ is at or below 0.1.

4. Dynamic mode-II delamination:
Setting $\cos\theta = 1$, we obtain

$$\varepsilon_c = \sqrt{\frac{2\gamma}{1-\alpha^2}} = \sqrt{\frac{2G_{c0}}{Eh(1-\alpha^2)}} \tag{162}$$

$$F_c = Ebh\varepsilon_c = b\sqrt{\frac{2EhG_{c0}}{1-\alpha^2}} \tag{163}$$

The derived expression for F_c corresponds to equation (51) from Sect. 4.1, in which the applied force is denoted as $F_c^{(i)}$, to emphasize that the result is valid for a rate-independent delamination model.

5. Dynamic peeling test at moderate speed, stiff sheet: This simplification is based on assumptions that $\alpha^2 \ll 1$ and $\gamma \ll 1$, but the derivation requires detailed justification. In analogy to case 2, but this time with a nonzero value of the relative crack speed α, it is assumed that the quadratic term in (151) is negligible with respect to the other terms. The reduced linear equation

$$2(1-\alpha^2)(1-\cos\theta)\varepsilon_c - 2(\gamma+\alpha^2(1-\cos\theta)) = 0 \tag{164}$$

leads to

$$\varepsilon_c = \frac{\gamma+\alpha^2(1-\cos\theta)}{(1-\alpha^2)(1-\cos\theta)} = \frac{\gamma}{(1-\alpha^2)(1-\cos\theta)} + \frac{\alpha^2}{1-\alpha^2} \tag{165}$$

The assumption that the quadratic term in (151) is negligible is justified if $\varepsilon_c \ll 1$. Looking at the resulting formula (165), we realize that the assumption is valid only if $\gamma \ll 1$ and $\alpha^2 \ll 1$. Consequently, as long as ε_c remains small, the factors $1-\alpha^2$ are very close to 1, and so (165) can be reduced to

$$\varepsilon_c = \frac{\gamma}{1-\cos\theta} + \alpha^2 \tag{166}$$

The corresponding force

$$F_c = Ebh\varepsilon_c = \frac{bG_{c0}}{1-\cos\theta} + \rho bh\dot{a}^2 \tag{167}$$

agrees with the result that is obtained directly from (144) if ε_c is set to zero and v is expressed from (146) with ε_c set to zero. For $\dot{a} = 0$, formula (167) reduces to (156), as expected. It is important to note that even though the static formula (156) is accurate whenever $G_{c0} \ll Eh$, its extension to the dynamic formula (167) is applicable only if the crack speed $\dot{a}$ is sufficiently small, such that $\dot{a}^2 \ll c^2$. If this is not the case, the strain cannot remain small and it is better to evaluate it from the full formula (152). Of course, for large strains it becomes questionable whether the linear elastic law can still be used. To reflect the true material behavior, one would need to replace the quadratic expression for the elastic energy (i.e., the second term on the right-hand side of (144)) by a more appropriate hyperelastic potential.

References

Allix O (2013) The bounded rate concept: a framework to deal with objective failure predictions in dynamic within a local constitutive model. Int J Damage Mech 22–6:808–828

Allix O, Deü J-F (1997) Delayed-damage modelling for fracture prediction of laminated composites under dynamic loading. Eng Trans 45:29–46

Burak G, Coker D (2016) Modeling of dynamic crack propagation using rate dependent interface model- Part B. Theor Appl Fract Mech 85:191–206

Cantwell WJ (1997) The influence of loading rate on the mode II interlaminar fracture toughness of composite materials. J Compos Mater 31:1364–80

Desmorat R, Chambart M, Gatuingt F, Guilbaud D (2010) Delay-active damage versus non-local enhancement for anisotropic damage dynamics computations with alternated loading. Eng Fract Mech 77:2294–315

Freund LB (1998) Dynamics fracture mechanics. Cambridge University Press, Cambridge

Gent AN, Kinloch AJ (1971) Adhesion of viscoelastic materials to rigid substrates. III. Energy criterion for failure. J Polym Sci Part A-2 Polym Phys 9:659–668

Guimard J-M, Allix O, Pechnik N, Thévenet P (2009) Characterization and modeling of rate effects in the dynamic propagation of mode-II delamination in composite laminates. Int J Fract 160(1):55–71

Kanninen MF, Popelar CH (1985) Advanced fracture mechanics. Oxford University Press, Oxford

Karac A, Blackman BRK, V. Cooper et al (2011) Modelling the fracture behaviour of adhesively-bonded joints as a function of test rate. Eng Fract Mech 78:973–989

Kendall K (1975) Thin-film peeling—the elastic term. J Phys D Appl Phys 8(13):1449–1452

Kubair DV, Geubelle PH, Huang YY (2003) Analysis of a rate-dependent cohesive model for dynamic crack propagation. Eng Fract Mech 70:685–704

Ravi-Chandar K, Knauss WG (1984) An experimental investigation into dynamic fracture - II. Microstructural aspects. Int J Fract 26:65–80

Smiley AJ, Pipes RB (1987) Rate effects on mode I interlaminar fracture toughness in composite materials. J Compos Mater 21:670–687

Smiley AJ, Pipes RB (1987) Rate sensitivity of mode II interlaminar fracture toughness in graphite epoxy and graphite peek composite materials. Compos Sci Technol 29–1:1–15

Tsai JL, Guo C, Sun CT (2001) Dynamic delamination fracture toughness in unidirectional polymeric composites. Compos Sci Technol 61:87–94

Valoroso N, Debruyne G, Laverne J (2014) A cohesive zone model with rate-sensitivity for fast crack propagation. Mech Res Commun 58(1):82–87

Zhou F, Molinari JF, Shioya T (2005) A rate-dependent cohesive model for simulating dynamic crack propagation in brittle materials. Eng Fract Mech 72:1383–1410